University of Padova

The Ph.D. School on Information Engineering

Department of Information Engineering

EEG source reconstruction accuracy and integration of simultaneous EEG-fMRI resting state data

PhD Thesis

Supervisor: Professor Alessandra Bertoldo

Co-Supervisor: Professor Antonino Vallesi

PhD Candidate:

Ilaria Mazzonetto

INDEX

ABSTRACT

The resting state functional magnetic resonance imaging (fMRI) approach has allowed to investigate the large scale organization of processing systems in the human brain, revealing that it can be viewed as an integrative network of functionally interacting regions. However, to date the neuronal basis of the fluctuations of the fMRI signal at rest are not fully understood, preventing the possibility to elucidate their functional role. In this scenario, the integration with information derived from electroencephalography (EEG) is very useful, since conversely from fMRI, EEG represents a direct measure of neuronal activity.

EEG-fMRI resting state studies investigating the correlation between fMRI signals and corresponding global EEG spectral characteristics in single spectral bands have provided a certain degree of inconsistency in the results. This may be due to the fact that the distinct functional networks involve more than a single frequency band and therefore analysis of simultaneous EEG/fMRI data should consider the whole frequency spectrum. A couple of studies have been performed in this directions but they either did not investigate how the scalp distribution of the EEG spectral metrics affects the patterns of correlations between EEG spectral dynamics and fMRI-derived resting state network or did not identify the specific scalp regions that specifically determined the pattern of observed results.

To overcome this gap, with the aim to identify specific spatio-spectral fingerprints of distinct networks, a first study was conducted using an analytical approach that allows to take into account the interplay between the different EEG frequency bands and the corresponding topographic distribution within each network. Specifically, this approach was applied to four sub-components of the Default Mode Network (DMN). Results revealed for the first time the presence of distinctive subcomponent-specific spatial-frequency patterns of correlation between the fMRI signal and EEG rhythm.

It should however be noted that spatial resolution of the EEG signal is too low to reliably infer about the location of the involved EEG sources. Therefore, a further step forward could be to try extending the findings of the first study in this direction by performing a source estimation study. Since it is not clear whether the 64 channels EEG system employed in the first study can provide adequate localization performance as regard our regions of interest, an investigation of the source reconstruction accuracy throughout the brain was performed in a second study. Specifically, the 64-channel montage was compared to 32-channel montage, the standard in the clinical practice, as well as to 128-channel montage and to 256-channel montage, considered as the upper reference point. Unlike previous studies, source performances were evaluated all over the cortical grey matter.

Results indicate that the localization of the cortical sources of the spatio-spectral fingerprints revealed by the previous study can be adequately inferred by using 64 channels, but a confirmation study with a 128, or even better 256, channels montage is needed. Moreover, particular attention should be paid to investigate deep regions, where localization performance is worse regardless the number of electrodes used.

This work was funded by the 7FP/2007-2013 European Research Council Starting grant LEX-MEA (GA no. 313692) to Antonino Vallesi.

1 Resting State EEG-fMRI acquisition

1.1 Resting State

In recent years, the temporal dynamics and associated topographies of a number of specific EEG-derived oscillations of neural activity in different frequency bands have been identified in the context of different types of task-related, “active” mental activity. For example, converging evidence from numerous studies using a variety of experimental paradigms and tasks (e.g., Stroop, flankers, Simon), data analysis techniques, and spatial and temporal filtering approaches, indicates that the (stimulus- and response-locked) modulation of theta oscillations (4-7 Hz) in the frontal regions is a sensitive and reliable electrophysiological marker for the need of cognitive control and the recruitment of the brain's action monitoring system. Indeed, transient event-related modulations of theta-band oscillations generated in the medial prefrontal cortex have been observed, in particular, during tasks that provoke a conflict between multiple available and competing behavioural and cognitive responses (Cohen and Donner 2013, Oehrn et al. 2014, Cavanagh and Frank 2014).

This is only one example of the numerous band-specific EEG spectral markers of task-related mental activity that have been discovered in the recent years. Importantly, multimodal EEG-fMRI studies have shown that trial-by-trial theta-related EEG measure of conflict-related cognitive processing significantly predicted both behavioural performance and the fMRI activity in brain regions

playing key roles in these processes (Debener et al. 2005, Lavallee et al. 2014). These results not only confirm that investigations of the dynamic coupling between EEG- and fMRI-derived signals provide a promising and powerful approach for the study of higher order brain processes, but they also highlight the importance of performing the spectral decomposition of EEG data when conducting multimodal EEG-fMRI analysis in order to elucidate the functional and behavioural meaning of BOLD oscillations.

By contrast, the electrophysiological correlates of spontaneous brain activity during the awake resting state (i.e., a task-free, relaxed wakefulness state) have been less well described and distinguished, despite their importance in clinical practice and the fact that the awake resting state have been the first condition that was ever investigated with EEG (Berger 1929). This is even more surprising when considering that the exploration of brain activity at rest has gained great interest in recent years in neuroscience, especially in the field of resting state fMRI. Indeed, since the seminal work by Biswal and colleagues (1995), there was a steady increase of the number of fMRI studies investigating the spontaneous fluctuations of BOLD signal during resting state (see figure 1.1).

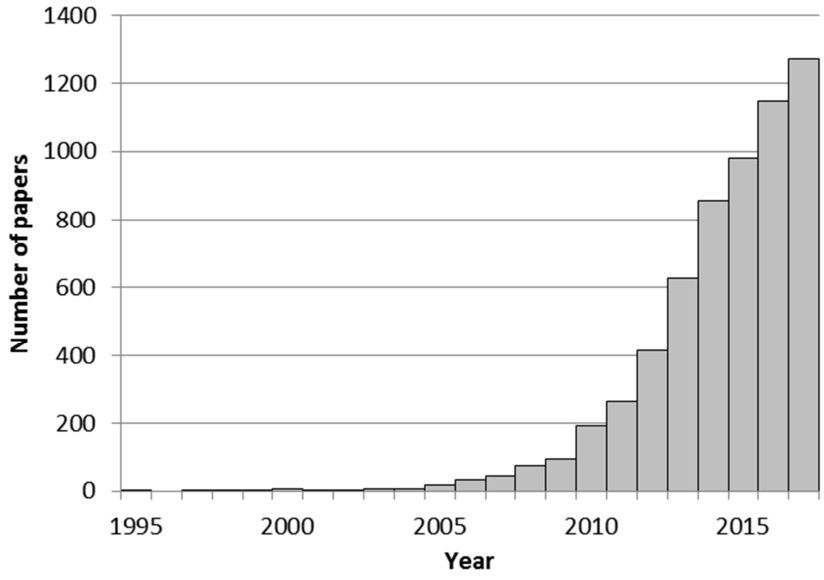

Figure 1.1: Number of resting state fMRI papers published each year since 1995, as revealed by the Pubmed results for the ["resting state" AND ("fMRI" OR "functional magnetic resonance")] query.

In that study, he demonstrated that BOLD signals at rest are temporally correlated within the somatomotor system and, thus, the slow spontaneous fluctuations of BOLD signal represents neural activity, rather than physiological noise as initially thought (Weisskoff et al. 1993, Purdon and Weisskoff 1998).

The resting state fMRI approach has been proven extremely useful to investigate the fundamental large scale organization of processing systems in the human brain, allowing to understand that brain can be viewed as a network of numerous different brain regions with specific functions, but which are constantly sharing information with each other; in other words, an integrative network of functionally interacting brain regions. Indeed, brain's spontaneous activity, as measured with fMRI-derived BOLD signal during resting state, has been shown to be organized into multiple, highly specific functional-anatomical networks, the so-called resting state networks (RSNs) (for reviews see Fox and Raichle 2007, Cole et al. 2010). As such, these RSNs are in turn organized to form a complex, higher-level network in which information is continuously computed and integrated by being transferred between structurally and functionally linked brain regions.

In particular, analytical approaches assessing functional connectivity, that is, the statistical association or dependency among two (or more) BOLD time-series from anatomically distinct brain locations (Friston 1994, Friston et al. 1996) have been extremely useful for resting state research (van den Heuvel and Hulshoff Pol 2010) and have greatly supported and contributed to the mounting scientific interest in the intrinsic neural activity of the brain. A number of reliable RSNs characterized by putative functional specificity have been described, such as, the visual, somatomotor, dorsal and ventral attention, default, cognitive control, limbic, auditory RSNs. These RSNs fluctuate at frequencies ranging between 0.01 and 0.1 Hz (Cordes et al. 2001), and strongly overlap with the corresponding networks of brain regions whose activity has been commonly shown to be modulated during active behavioural tasks (Smith et al. 2009). More importantly, resting-state research, by providing information about brain's functional integration, represent an useful conceptual complement to the inferences made from task-related functional data, which gives information about brain's functional segregation, that

is, the specialization of different brain regions for a given function. As a consequence of this, the resting state approach is increasingly being utilized across multiple fields of neuroscience (and also in medical sciences), to further inform our understanding of the functional organization of brain activity. Indeed, abnormal deviations from the normal pattern of functional connectivity at a system level are observed in a number of clinically relevant conditions, including varying states of consciousness, both physiological and pathological (e.g., Heine et al. 2012), and even neurological (e.g., Rombouts et al. 2005) and psychiatric disorders (e.g. Greicius et al. 2007).

It is interesting here to note that the perhaps more studied and fundamental of the RSNs, the so-called default-mode network (DMN), is also the only one that had, at the time, unexpected brain topography and functional characteristics. Indeed, the DMN is composed by brain regions that had not previously been documented as a "proper functional system" as opposed to, for example, the motor or visual systems. Moreover, the DMN was first identified from a large meta-analysis of published PET data by the Raichle's group (Shulman et al. 1997, note that the "default mode" name was firstly proposed in a later paper by the same group, Raichle et al. 2001). In this study, the authors revealed a reliable decrement of the neural activity in a specific and consistent set of brain areas during the execution of a cognitive task. The existence of such a DMN was soon confirmed in later meta-analyses (Binder et al. 1999, Mazoyer et al. 2001) and by an fMRI study by Greicius and colleagues (2003) and, to date, by a tremendous number of studies using a variety of analysis methods (e.g., Sasai et al. 2012, Liu et al. 2017, Pasquale et al. 2010, Jerbi et al. 2010). Moreover, evidence of DMN-equivalent RSNs in other mammals have been provided in more recent years (monkey, Mantini et al. 2011b, cat, Popa, Popescu and Pare 2009, and even mouse, White et al. 2011). Interestingly, subsequent studies have suggested that the DMN can indeed be further decomposed into distinct sub-networks based on their specific functional characteristics (e.g., Whitfield-Gabrieli et al. 2011, Andrews-Hanna et al. 2010).

However, to date the neuronal basis of the low-frequency fluctuations of the BOLD signal are not fully understood, and the elucidation of the neurophysiological underpinnings of the RSNs, and of the neuronal dynamics underlying brain's spontaneous activity more generally, is a critical step needed to understand their functional role. Contributing to this problem is the fact that BOLD signal is an indirect measure of neuronal activity related to hemodynamic (Ogawa et al. 1992), and may thus reflect other related physiologic properties such as cerebrovascular variations (Kennerley et al. 2010). Therefore, the neurophysiological basis of functional connectivity between spatially separate brain regions cannot be comprehensively investigated using the fMRI technique. By contrast, electroencephalography (EEG) is a direct measure of neuronal activity, and it can even furnish an effective measure of neuronal firing (e.g., Nunez and Silberstein 2000, Nunez and Srinivasan 2006, Whittingstall and Logothetis 2009). It should also be noted that, despite representing different aspects of brain activity, EEG- and fMRI-derived signals have been shown to have a common origin (Logothetis et al. 2001). Therefore, the combination of EEG and fMRI can yield insights that are not accessible to one modality alone. The simultaneous EEG-fMRI multimodal approach has also received attention due to the complementary temporal and spatial resolutions inherent to each technique, as the EEG technique poses the problem of source localization.

The first EEG-fMRI studies investigating healthy volunteers at rest were focused on the BOLD correlates of the so-called alpha rhythm (Berger 1929), the most prominent EEG feature during the awake resting state, which was characterized by oscillations in the 8-12 Hz frequency band most noticeable over posterior regions of the scalp. Berger also noticed a desynchronization of these alpha waves due to engagement in attention-demanding tasks. Consistently with Berger's observations, the first EEG-fMRI studies investigating the BOLD correlates of spontaneous fluctuations in alpha activity (Goldman et al. 2001, Goldman et al. 2002, Moosmann et al. 2003, Laufs et al. 2003b, Laufs et al. 2003a) have shown that the expected posterior regions, but also other brain regions across the cortex, showed BOLD activity that was negatively correlated with posterior alpha fluctuations. In particular, Laufs and colleagues (2003b) found that the alpha desynchronization

was correlated with the BOLD activity in a frontal-parietal network that was previously (and independently) characterized as an attentional system. Similar findings were also observed in a study by Mantini and colleagues (2007b).

However, there is a certain degree of inconsistency in the results from these and other EEG-fMRI studies investigating the correlation between BOLD signals and corresponding global EEG spectral characteristics in single spectral bands (Laufs 2008), such as the theta, alpha, and beta ones (Goldman et al. 2002, Laufs et al. 2003a, Laufs et al. 2003b, Moosmann et al. 2003, Feige et al. 2005, Goncalves et al. 2006, Scheeringa et al. 2008). As highlighted by Mantini and colleagues (2007b), however, this can be explained by the fact that "From a theoretical standpoint […], the assumption that a single cerebral rhythm is associated with a specific cerebral functional network is not likely" (Mantini et al. 2007b, p. 13170), suggesting that multiple frequency bands should be involved in distinct functional networks (see also Laufs et al. 2006), and, thus, "analysis of simultaneous EEG/fMRI data requires methods that consider the whole frequency spectrum rather than single frequency bands" (Mantini et al. 2007b, p. 13171).

The above-mentioned study by Mantini and colleagues was indeed the first one to investigate in a comprehensive and systematic way the relationship between coherent low-frequency fluctuations of BOLD signal and oscillations of the neuronal electrical activity in different EEG frequency bands. In particular, they first identified six RSNs by analyzing the independent spatio-temporal patterns in hemodynamic activity using independent component analysis (ICA). Next, they directly correlated the time courses of different RSNs with the time courses of EEG spectral fluctuations across delta, theta, alpha, beta, and gamma bands averaged over all the EEG channels. The results of this study revealed that each RSN was associated with a specific neurophysiological spectral signature, a unique pattern of correlations across frequency bands.

Despite the importance of this study cannot be questioned, it shares with earlier EEG-fMRI resting state studies an crucial limitation, that is, it did not allow to

understand the impact of the scalp distribution of the EEG spectral metrics in shaping the patterns of correlations between EEG spectral dynamics and fMRI-derived RSNs. Indeed, using single (at the spatial level) EEG spectral metrics, such as the power averaged over all scalp channels (Mantini et al. 2007b) or extracted by single of few channels (Goldman et al. 2002, Laufs et al. 2003a, Laufs et al. 2003b) causes the loss of spatial specificity of electrical oscillations, a source of information about EEG spectral activity that is essential to appreciate its functional meaning. Indeed, as highlighted by Jann and colleagues (2010), the scalp distribution of spectral power "is an important and sensitive marker for changes of brain functional state, on a local and global level. Deviations from the resting state during task execution or alterations caused by disease are often local, i.e., at delimited scalp locations […] and changes of the distribution of EEG rhythms are well-established markers for changes of brain state" (Jann et al. 2010, p. 1).

Despite Jann et al. themselves (2010) tried to tackle this issue, they too failed to reveal whether RSNs activity can be related to EEG spectral oscillations in specific scalp regions. They assessed the topographic association of EEG spectral dynamics and RSNs fluctuations by means of the statistical approaches called EEG covariance mapping (Koenig et al. 2008) and topographic ANOVA (TANOVA, Koenig and Melie-Garcia 2009, Strik et al. 1998). They found significant and specific RSN-related scalp distributions of the spectral power across frequencies or, in other words, significant frequency-dependent differences between EEG-fMRI covariance maps distributed over the scalp, both across bands and within each single frequency band. However, these statistical tests, which compare entire scalp distributions, could not identify the scalp regions that specifically determined the pattern of observed results and were also not followed by specific post-hoc tests aimed to determine the interplay between the different frequency bands in driving the observed results.

1.2 Aim of the study

The aim of the present study is to fill the gap in the literature that was presented in the previous section. To this aim, the patterns of correlations between EEG spectral dynamics and fMRI-derived RSNs were investigated by 1) analyzing the spectral dynamics in the different frequency bands composing the entire (1-45 Hz) power spectrum, 2) analyzing the channel-by-channel distribution of spectral metrics, so to cover the entire scalp, and, importantly, 3) using an analytical approach and a state-of-the-art data-driven statistical method that allows to take into account the interplay between different EEG frequency bands (i.e., to compare their specific patterns of correlations with RSN activity) and the corresponding topographic distribution within each RSN, but also to compare the specific RSN-related topographic association of EEG spectral dynamics and BOLD fluctuations to identify specific spatio-spectral fingerprints of distinct RSNs. As an applicative proof of concept, this analytical approach was applied to the sub-networks composing the DMN in order to verify its validity and potential to identify even the subtle differences in the specific spatio-spectral correlates of related sub-RSNs.

1.3 Technical challenges in EEG-fMRI simultaneous acquisition

Apart from the specific issues detailed in the previous sections, the simultaneous registration of EEG and fMRI signals poses a number of technical challenges.

To measure EEG inside the scanner, some technical and safety related issues should be considered. The main sources of artifacts that affect EEG data are: 1) the static field (B_0), namely the field strenght of the scanner (which is always there, even when not scanning); 2) the rapidly changing magnetic fields (B_1), also called "gradient switching", which refer to the spatial gradients generated in the *x*, *y* and *z* direction; 3) the Radio Frequency (RF), namely pulses from the trasmit coil,

always present during scanning; and 4) the heart pulse, namely movements deriving from the cardiac cycle.

During a simultaneous EEG-fMRI acquisition, subject lies supine in the magnet wearing an electrode cap. Therefore, cap, electrodes and electrode leads are exposed to the static magnetic field of the scanner, to quickly variable magnetic fields generated by gradient switching and to radio frequency energy emitted during the MRI acquisitions (Ullsperger and Debener 2010). Since both electrodes and leads are made up of electrically conducting materials, in accord with Faraday's law, any changes in the magnetic field, both induced by the switching of the magnetic gradients and by subject or cable movement, induces a current flowing through them (Hill et al. 1995, Lemieux et al. 1997). The induced flux of current results in a variation of the electric potential that is measured along with the brain electrical activity as an artifact. The amplitude and rate of change of this gradient artifact (GA) superimposed signal are much higher than those of the EEG, up to two orders of magnitude for the amplitude and three for the rate of change (Allen, Josephs and Turner 2000, Ritter et al. 2007). Specifically, the amplitude and frequency characteristics of the GA depend on factors related to the MRI environment, like the strength and slew rate of the gradient, as well as to the EEG system, like the filter characteristics of the amplifier and the length of the leads. Concerning long leads, they tend to have a more antenna-like behaviours and may pass through inhomogeneous portions of the magnetic field increasing the magnetic induction. The fundamental frequencies of the GA are the slice acquisition frequency of fMRI sequence and its harmonics. For example, with a TR = 2 s and a fMRI volume of 30 slices, the fundamental frequency will be at 15 Hz and the harmonics at 30 Hz, 45 Hz and so on. Another important frequency is the frequency of gradient switching during the spatial encoding within a slice. For example, if the lines per image are 64, there will be a peak at frequency $64 \times 15 = 960$ Hz (Ullsperger and Debener 2010). This peak does not directly affect the band of interest of the EEG, but without an antialiasing filter it could compromise the lower frequency during the EEG sampling. Since the gradient artifact is technical in nature, repetitive, predictable and temporally stable (synchronized with the repetition time), an accurate trigger and interface with the scanner allows the

artifact handling and removal. Due to electrode and cable arrangement within the cap and their position in the gradient field, the GA varies in amplitude and shape across EEG channels. Therefore, the gradient artifact calculation and correction is done per channel. Artifacts induced in the EEG by the scanning process have a strong deterministic component, therefore their correction is generally considered a resolvable problem (Allen et al. 2000, Niazy et al. 2005).

After GA, another important artifact distorting the EEG is the heart pulse-related artifact (cardioballistographic artifact, BCG). It is a distortion of the EEG signal due to movement related to the cardiac cycle in the magnetic field. It has a physiological rather than a technical nature. Motion related to cardiac activity induces electromotive forces in the circuit formed by the EEG leads and the subject, which is caputered by the amplifier. The sources of this artifact are multiple: axial head rotation (rocking, nodding head motion, Anami et al., 2003), the pulsatile properties of the blood vessels, the acceleration of blood, which is electrically conductive (Hall effect). This artifact is related to the static field (B0), therefore it is always present. It is irregular both between and within participants. Accordingly, the BCG is subject to substantial temporal fluctuations, making its removal challenging. Importantly, it contributes to the low frequency portion of the EEG signal (< 15 Hz). A concurrent recording of the electrocardiogram (ECG) with the EEG reveals that the periodic distortion present in most EEG channels is related to the cardiac cycle.

During a simultaneous acquisition, one of the hazards for the subject is the heating of some scalp sites due to the dissipation of the RF energy. Positioning the EEG electrode cap on the scalp and creating a contact between the electrodes and the scalp tissue by means of a conductive gel creates a conductive surface with high thermal resistance. RF energy induces surface current densities that shield the inside surface of the skull. So, to achieve the desired flip angle and a good quality image, higher RF energy is necessary. However, this energy is dissipated as warming at the point of the highest thermal resistance, that is, the scalp/gel border. It can be showed that temperature changes induced by the sequences depend on their RF energy

emitted, which in turn reflects the number of RF excitation and inversion pulses (Ullsperger and Debener 2010).

Another issue to be considered is RF energy coupling onto cable loops. The induction effect can even melt the sheath of the cable at the crossing points. This effect, although exacerbated in the presence of loops, could affect any cable with length and shape such that it becomes resonant at the particular MR scanner's Larmor frequency (42.58 MHz/T) or at any related harmonic (Ullsperger and Debener 2010).

Obviously, leads and electrodes must be made from non-ferromagnetic materials; usually the former are produced in carbon fibres or stranded copper, whereas the latter in sintered Ag/AgCl or gold. To reduce the risk of RF-induced cable heating, RF shielding resistors are conductively glued to the electrodes surface. Their resistivity varies between 5 and 15 kΩ in function of the field strength and the length of the leads (Lemieux et al. 1997). Since the induced effect in a conductive loop is proportional to the loop area, the area of any loop that could not be avoided should be minimized. Therefore, electrode leads are bunched together and then twisted along the path toward the input of the amplifier. This solution keeps the leads close together minimising the loop area and results in a cancellation of the currents induced in adjacent leads (Mulert and Lemieux 2009). Moreover, to prevent the leads movement they are fixed to the cap. Particular attention should also be paid to the peripheral leads such as that used to record electrocardiogram (ECG). Since it is longer than other leads and crosses inhomogeneous parts of the magnetic field, it is exposed to a greater MR gradient and RF energy induction. Therefore, differently from the scalp electrodes leads, it is upholstered with a heat resistant tube. The electrode is also covered by means of a plastic holder to avoid the direct contact with the skin and its RF shielding resistor is 15 kΩ (Ullsperger and Debener 2010).

EEG system can be arranged in the scanner control room or inside the bore. If the equipment is located outside the scanner room, it does not have to meet MR compatibility and MR safety criteria. On the other hand, the leads have to be very long to cover the distance between the amplifier and the electrodes on the subject scalp. In addition to the gradient and RF induction related issues, longer cables entail also a signal decay and their movement are not easily avoidable. But, the biggest problem is that they need to pass through the filter panel into the MR control room by means of a conduit. In this way, an electrical connection between scanner and control room is made, which can lead to RF energy leakage into the MR chamber. When EEG system is placed inside the bore, leads are shorter and, thus, MR gradient, RF signal and cable movement artifacts are reduced. Moreover, in this situation, signal can be transmitted from the amplifiers to the recording computer, in the control room, by means of fibre optical leads with no risk of creating an RF leak. In this situation, amplifiers are battery powered and are enclosed in a MR shielding box, where there are also RF filters and two channel fibre optical links. Communications with the recording software are made through an USB interface that contains the electronically critical components like the electronics of the acquisition clock, the logic for integrating external events, and the circuit for the synchronization with an external clock signal (Ullsperger and Debener 2010).

To limit the EEG artifact related to MRI environment, lead movements should be limited. Their movements can be due to the BCG (Allen et al. 2000), subject's head movements, and vibrations induced by the cryogenic pump and by the gradient switching itself (Garreffa et al. 2004). These vibrations affect also the amplifier (when it is inside the bore) and the electrodes leads it is connected to, intensifying the induced oscillations. To minimise artifacts, leads are usually weighed down with sandbags, paddings are put under the amplifier, and the subject is immobilized as much as possible with cushions placed laterally and under his head.

The amplifier of an MR-compatible EEG system must be tuned differently with respect to those of a classic EEG system, because of gradient switching effect

indeed, the input signal is extremely different compared to the signal usually recorded. The gradient artifact has a broad spectrum, extended from the low frequencies to thousand Hertz. Containing the gradient energy within the bandwidth of the amplifier and avoiding aliasing effects is not trivial. The most common MR compatible EEG systems sample the signal at 5000 Hz, so that, in accordance with the Nyquist theorem, the highest representable frequency in the data is 2500 Hz. However, gradient artifacts power spectrum has peaks also beyond this frequency. An analog band limiting filter is useful to reduce the signal energy avoiding aliasing artifacts (Ullsperger and Debener 2010).

Another important aspect to consider is the maximal amplifier gain to prevent risk of amplifier saturation. Of course, it depends on the AD bit count and its dynamic range, but gradient artifacts should also be considered, since its amplitude and frequency are several orders bigger than those of the classical EEG.

To correct the gradient artifact from the EEG data, the onset of each gradient activity should be known. This is not a matter, since MR scanners have in their console a TTL or fiber optical output which send a pulse when the slice or volume acquisition starts. The EEG system receives the onset pulse and saves it with its next data point. So, with the typical data acquisition rate of 500 Hz, the marker could be saved at most under 2 ms later. EEG data are then segmented based on the marker position and averaged to build the artifact template. The problem is that given the high frequency content of the gradient artifact, its shape changes along the 2 ms. Therefore, data that are averaged are not aligned. To avoid this inflated standard deviation at the gradient onset points, the sampling rate is increased, usually to 5000 Hz. Even at this higher sample rate, temporal jitter in the EEG sampling, although with minor size, are still present. A valid alternative is to have the EEG acquisition clock drives by the 10 MHz MR system clock. MR scanners indeed provided on commonly used connector a clock signal that is collected by the synchronization hardware. Signal is then stabilized and transported from the MR system electronics cabinet to the scanner control room. Stabilization is needed to prevent decay or slurring of the

signal edges, important for high frequency phase alignment. Finally a clock divider circuit down sample the MR signal into a clock signal that can be used by the EEG amplifier (Ullsperger and Debener 2010).

1.4 Participants and resting acquisition

Twenty-two healthy young people took part in the experiment in exchange for payment (about 8 € per hour). Data from two participants were discarded because of excessive head movements (see paragraph 2.3). Therefore, the results are reported here for 20 participants (12 female; mean age: 23 years; age range: 20 – 28 years). They were all right-handed, according to the Edinburgh Handedness Inventory (Oldfield 1971) and reported normal or corrected-to-normal visual acuity (MRI-compatible glasses were used when appropriate). The study was approved by the Bioethical Committee of the Azienda Ospedaliera di Padova and was conducted in accordance with the guidelines of the Declaration of Helsinki. All participants signed a written informed consent prior to their participation. The acquisition protocol included resting-state and task-related simultaneous EEG-fMRI, and a structural image. The task-related activity analysis is not discussed in this thesis and has already been published in (Tarantino et al. 2017). In the resting state session, subjects were asked to lie inside the scanner, to move as little as possible, and to fix a cross in the centre of a screen. The screen was placed at the rear of the bore and was visible to the participants through a double mirror system mounted on the head coil.

1.4.1 MRI acquisition

Structural and functional images were acquired using a 3T Ingenia Philips whole body scanner (Philips Medical Systems, Best, The Netherlands) equipped with a 32-channel head-coil, at the Neuroradiology Unit of the University Hospital of Padova, Italy.

Functional data were obtained using a whole head T2∗-weighted echo-planar image (EPI) sequences (repetition time, TR: 2000 ms; echo time, TE: 35 ms; 25 axial slices with ascending acquisition; voxel size: 2.4 × 2.4 × 4.8 mm; flip angle, FA: 90°; field of view, FOV: 230 mm, acquisition matrix: 84 × 80; SENSE factor: 2 in anterior-posterior direction). The functional time series consisted of 200 volumes, equivalent to 400 s. At the start of each volume acquisition, a transistor–transistor logic (TTL) pulse was sent from the MRI scanner to the EEG recording system. Special care was taken to ensure that frontal areas and cerebellum were included in the volume. In order to avoid head movement, small foam cushions and sponge pads were placed around the participant's head. Subjects also wore earplugs to reduce acoustic noise.

After functional session, high-resolution T1-weighted anatomical images (TR/TE: 8.1/3.7; 180 sagittal slices; FA: 8°; voxel size: 0.49 × 0.49 × 1 mm; FOV: 220 mm; acquisition matrix: 220 × 220) were acquired.

1.4.2 EEG acquisition

The EEG signal was recorded using an MR-compatible system (Brain Products, Munich, Germany), connected to 64 sintered Ag/AgCl ring electrodes and mounted on an elastic cap (BrainCap MR) according to the extended 10–20 system. Electrocardiographic (ECG) signal was acquired by means of an electrode placed in the middle of participants' back, approximately 4 cm left to the spine. Channels FCz and AFz served as online reference and ground, respectively. Acquisition did not start until electrodes impedance was set at values less than 5 kΩ. The EEG signal was band-pass filtered between 0.016 and 250 Hz and digitized at a sampling rate of 5 kHz. The amplifiers were placed at the rear of the scanner bore such that connection with subject's EEG cap could be realized by means of short cables. To minimize artifacts induced by movements and vibrations, both amplifiers and cables were fixed with sandbags.

1.5 MRI preprocessing

Anatomical images were bias-field corrected and skull stripped with FreeSurfer (Fischl 2012) software suite version 5.3.0 (Massachusetts General Hospital, Harvard Medical School; http://surfer.nmr.mgh.harvard.edu). A non-linear transformation from T1-weigthed images to standard Montreal Neurological Institute (MNI) template was estimated using FSL (FMRIB Software Library, version 5.0.7) (Smith et al. 2004).

This software was also used to preprocess individual functional data. To eliminate the fMRI signal decay associated with magnetization reaching equilibrium, the first seven volumes were discarded. Afterwards, functional data were slice-timing corrected using the middle slice as the reference frame and rigidly realigned to the first volume. To quantify participants' head movements during the acquisition, framewise displacement (FD) was calculated for each participant (Power et al. 2012). This index represents the sum of the absolute values of the derivatives of the translational and rotational realignment parameters. Subjects with mean FD above two standard deviations from the mean of all subjects (group mean = 0.09 mm, standard deviation = 0.02 mm) were excluded.

To perform normalization, the 12-parameter affine transformation from the first volume of the functional data to the anatomical image was combined with the transformation from the anatomical image to the template and applied to all volumes. In the same operation, data were also resliced to 2 × 2 × 2 mm voxels. After grand mean scaling, the functional images were temporally filtered with a high-pass filter with cut-off frequency of 0.01 Hz and spatially smoothed using a Gaussian kernel with a full-width at half-maximum (FWHM) of 4 mm.

FMRI data of all subjects were decomposed into 50 functional networks using a group-level spatial ICA as implemented in the GIFT toolbox (http://mialab.mrn.org/software/gift/). The number of components was taken as the mean of the estimated components for each dataset using the minimum description

length criterion modified to account for spatial correlation (Li, Adali and Calhoun 2007). Before performing the ICA, Principal Component Analysis (PCA) was used in a two-step process to reduce the dimensionality of the data. The first step was applied to each individual dataset, which was reduced to its first 75 principal components. The second step was applied to the group data and 50 components were retained. The Infomax ICA algorithm (Bell and Sejnowski 1995) was run 10 times in ICASSO (http://www.cis.hut.fi/projects/ica/icasso/) (Himberg, Hyvarinen and Esposito 2004) to identify the most stable components across all iterations. Since Resting State Networks (RSNs) are characterized by low frequency fluctuations (Cordes et al. 2001), components whose power spectrum of their associated time course felt 50 % or more above a high frequency range (> 0.1 Hz) were rejected (Greicius et al. 2004). Then, component of interests were selected by visual inspection based on previous literatures (Beckmann et al. 2005, Allen et al. 2014) and back-reconstructed through dual regression (Filippini et al. 2009) to produce individual RSNs spatial maps and time courses. The dual regression proceeds in two steps. For each subjects, group spatial maps are regressed against fMRI data to obtain one time course for each component. Then, time courses are regressed against fMRI data to obtain spatial maps of each network.

Before proceeding with network analysis, a multiple regression of the movement parameters was performed on the time courses of the 26 selected networks, for each subject separately. Indeed, although previous studies (Kochiyama et al. 2005, McKeown, Hansen and Sejnowsk 2003) have been demonstrated that spatial ICA detects motion related components that can be further removed from the data, given the spatial non-stationarity of movements, residual motion related variance cannot be completely discarded (Allen et al. 2014).

The next step aimed to distinguish sub-networks belonging to larger major RSNs characterized by putative functional specificity, such as, the visual, somatomotor, dorsal and ventral attention, default, cognitive control, limbic, auditory RSNs. In particular interest was in distinguishing the different sub-networks composing the so-called default-mode network (DMN). Therefore, groups of RSNs that are alike based on similarities in their BOLD time courses were identified by performing an

agglomerative hierarchical cluster analysis using the Ward's linkage method (variance-minimizing approach, Ward Jr 1963) based on the Euclidean distance metric. This procedure generates a hierarchy of clusters represented as a dendrogram (Johnson 1967), a binary tree where each node is associated with the higher-level cluster obtained by merging its two children clusters.

1.6 EEG preprocessing

The EEG data preprocessing was performed using EEGLAB 13.6.5 (Delorme and Makeig 2004) and Matlab R2016b (The MathWorks, Natick, 2016).

The gradient artifact (GA) was removed using the fMRI artifact slice template removal (FASTR) algorithm implemented in the FMRIB plug-in (Niazy et al. 2005). Briefly, contaminated data were upsampled to a sampling rate of 20 kHz and locations of triggers sent by MRI machine at the beginning of each volume acquisition were adjusted with respect to a reference segment. Here "segment" or "artifact" are referred to EEG data between two consecutive trigger positions. To do this, all artifacts, save the first one that is taken as reference, were shifted forward and backward and each time correlation with the reference was calculated. For a given triggers, the new position was one that maximized correlation. This *a posteriori* synchronization was fundamental for the next step in which an artifact template was created. Indeed, due to the fact that MRI and EEG system were driven by distinct clocks, locations of trigger relative to the artifact could be not aligned across the volumes. For each segment of corrupted data, a template was built by averaging *n* artifacts (20 in this study) around current position and then it was subtracted from the data. However, only sudden changes in the waveform of gradient artifact (due to movement for example) were taken into account, in this way. To remove residual variance related to slow variations of the shape, a set of basis function with PCA were derived from the data previously cleaned. This optimal basis set (OBS), whose number of principal components was determined based on the amount of variance explained, was then fitted to, and subtracted from,

each segment. A further step of adaptive noise cancellation filter was considered to remove any remaining residuals. In this study, the last two steps were performed only on brain channels, since on ECG channel they resulted in the loss of data. Essentially, their application warped so much the signal that R peaks were no longer detectable. At the end, GA-free signal was brought back to its original sample rate.

Removal of ballistocardiographic (BCG) artifact was usually carried out by means of adaptive average subtraction (Allen et al. 2000) or optimal basis set (Niazy et al. 2005). Both these methods rely on the assumption that BCG artifacts follow the R peaks of ECG trace with a fix delay of around 200 ms. Recently, instead, it has been demonstrated that the delay of BCG artifact with respect to ECG is variable (Oh et al. 2014, Iannotti et al. 2015, Marino et al. 2017) and so the commonly used methods to its removal could be suboptimal. Therefore, in order to take the variable delay into account, the BCG was here removed using a semiautomatic procedure implemented in Matlab. As an initial step, the QRS complexes of every heart pulse were automatically detected on the ECG channel. To ensure the correct identification of all R peaks, the result was visually inspected and eventually adjusted. PCA was applied on the continuous brain recording and the first principal component was taken as an estimate of the artifact related to cardiac activity. On this signal, the highest peak in a time window from 100 to 300 ms after R peak was marked as an occurrence of BCG artifact. EEG signal was then epoched based on BCG peaks. Since heart rate is not constant along the acquisition, epochs were interpolated to have all the same length. PCA was performed and the first three components (including the mean effect) were used as an OBS to remove artifact. Clean epochs were then brought back to the original length and concatenated in time. To avoid discontinuity, the segment spanning 100 points before and after each conjunction point was replaced with its smoothed version obtained with a robust local regression using weighted linear least squares and a 2^{nd} degree polynomial mode.

In order to get rid of line and high frequency noise and as a preprocessing step for ICA (Winkler et al. 2015), data were bandpass filtered by applying a zero-phase

Hamming windowed sinc FIR filter with cut-off frequencies of 1.5 and 49.5 Hz (bandwidth = 1 Hz, ripple = 0.0022). The EEG signal was then down-sampled to 250 Hz.

A first rough automatic detection of bad channel was performed based on their correlation (computed in time window of 1 s) with all the other channels. A channel was rejected if the 98th percentile of the absolute values of the correlations was less than 0.4 for more than 1% of the windows (Bigdely-Shamlo et al. 2015). Next, a finer channel rejection procedure was also conducted (Bigdely-Shamlo et al. 2015). At this step, channels that correlated, in absolute value, less than 0.7 with their robust estimate (computed on the basis of a 100-point random sample consensus procedure) for more than 25% of the recording were removed.

The MRI artifact residuals, ocular movements and muscular activity were removed by means of Independent Component Analysis (Debener et al. 2007), based on fast fixed-point ICA (FastICA) algorithm (http://research.ics.aalto.fi/ica/fastica) using a deflation approach and hyperbolic tangent as contrast function (Mantini et al. 2011a). Independent components that did not represent brain activity were automatically pinpointed and then confirmed as artifacts by visual inspection of the time course along with power spectrum and scalp topography. In particular, GA-related components were identified based on the presence in their power spectrum of peaks at frequency of 12.5 Hz (number of slices in a volume/TR) and harmonics. BCG-related components were identified based on a correlation bigger than 0.2 with the BCG signal (previously identified as the first principal component of the GA–free continuous recordings) (Mantini et al. 2007a). Concerning ocular artifacts, components were selected depending on kurtosis values bigger than 13 (blinks) and specific scalp topographies (saccades) (Liu et al. 2017, Viola et al. 2009). Muscular activity-related components were selected among those having a ratio of high frequency (> 25 Hz) content to low frequency content bigger than one.

Removed channels were then interpolated using spherical splines (Perrin et al. 1989) and data were re-referenced to the average of all electrodes, with the exception of the ECG channel, which was discarded.

EEG data were segmented into epochs of 2000 ms, according to the TR of fMRI acquisition, and power spectrum was computed for each of them using a Welch's overlapped segment averaging estimator to obtain a 0.5 Hz resolution (250-points Hamming window, 500-points discrete Fourier transform, 125 points of overlap). From the absolute power spectrum, relative power for the delta (1-3.5 Hz), theta (4-7 Hz), alpha (7.5–12.5 Hz), beta (13–24 Hz) and gamma (24.5-45 Hz) were calculated. Moreover, to have quantitative measures reflecting temporal changes of attention and vigilance levels during resting state condition, the alpha/theta and beta/alpha ratios were also computed (Laufs et al. 2006, Ambrosini and Vallesi 2016).

For each specific rhythm (and ratio), relative powers along the epochs were concatenated and the resulting time serie was convolved with the standard SPM12 (http://www.fil.ion.ucl.ac.uk/spm/software/spm12/) hemodynamic response function (onset = 0 s, delay of response relative to onset = 6 s, delay of undershoot relative to onset = 16 s, dispersion of response = 1 s, dispersion of undershoot = 1 s, ratio of response to undershoot = 6 s, length of kernel = 32 s). Finally, the first 7 points were discarded as done for fMRI data.

1.7 EEG-fMRI integration

To analyze the correspondence between neuronal rhythms and RSNs, for each subject and channel, the RSNs average signals were correlated to the different band-power time series. Correlations were then Fisher-transformed and analyzed at group level. Given a specific network and an EEG channel waveforms, the statistical significance of their correlation among subjects was first evaluated with a two-tailed one-sample *t*-test. The significance level was corrected for multiple

comparisons by using the 'threshold-free cluster-enhancement' technique followed by permutation test as implemented in the ept_TFCE-matlab toolbox (https://github.com/Mensen/ept_TFCE-matlab) with a family-wise alpha level of 0.05 (Mensen and Khatami 2013). A total of 64 tests (repeated measure ANOVAs), one for each channel used for the EEG recording, and 2500 permutations were performed. Therefore, the most extreme *t*-values in each of the 2500 permutations after TFCE transformation were used to estimate the *t* distribution under the null hypothesis against which to compare the 64 observed *t*-values. TFCE considered a trade-off between sensitivity to intense local effect versus smaller amplitude effect but with a more diffusion over the scalp and frequencies. It had been shown that it provided a strong control of the type-I family-wise error rate and thus a great degree of certainty that both the sign and the spatial localization of a given effect were reliable (Mensen and Khatami 2013).

The same analyses were also performed with the beta/alpha and alpha/theta ratios.

Then, to detect specific inter-band topographical patterns of significant EEG-fMRI relationship, for each network the Fisher-transformed correlation coefficients were analyzed over the sensor space by means of mass-univariate analysis (ANOVA) with the five bands as factor (TFCE corrected, $p < 0.05$).

After the ANOVA, in order to assess the differences in how a resting state network correlated with the five frequency bands, ten *post hoc* pairwise *t*-tests were performed (TFCE corrected, $p < 0.05$). These evaluations were only computed in the channels belonging to cluster where *F* achieved the necessary level of statistical significance.

Finally, to investigate the presence of specific spatio-spectral fingerprints of distinct RSNs, a further mass univariate ANOVA in sensor-frequency space with the networks of interest as a factor were performed. The total comparisons were 320, corresponding to the combination of the 64 channels used for the EEG recording and the five bands of interest.

1.8 Results

1.8.1 EEG and fMRI

Subcomponents of the networks of interest were identified by means of the hierarchical clustering. This analysis revealed that four ICs components with similar time courses were grouped together into an extended RSN that could be considered, based on the spatial maps of the four lower-level RSNs, as the Default Mode Network. The spatial maps and the average signals of the subcomponents were illustrated in figure 1.2. The first network included the middle and the medial part of the orbitofrontal cortex, the anterior part of the cingulum and the medial part of the superior frontal cortex. It was labelled Self+Rest. The second network, called Rest, was constituted by the middle temporal and the angular gyrus, the cuneus, the precuneus, the posterior part of the cingulum and the middle frontal gyrus. The third network, called Self, mostly included the medial part of the superior frontal gyrus anteriorly. Finally, the fourth network, called Rest2, extended to the angular gyrus, inferior parietal lobe, the middle part of the cingulum, the middle frontal gyrus and the medial part of the superior frontal cortex posteriorly. The four sub-networks of the DMN were labelled according to a recent study by Whitfield-Gabrieli and colleagues (2011), which proposed a similar decomposition of the DMN based on the functional associations and dissociations between different sub-networks of the DMN: Self+Rest subcomponent involved regions that were involved in both self-reference and rest processes; Rest and Rest2 were more related to purely rest process; and Self regions were preferentially engaged during explicit self-reference process.

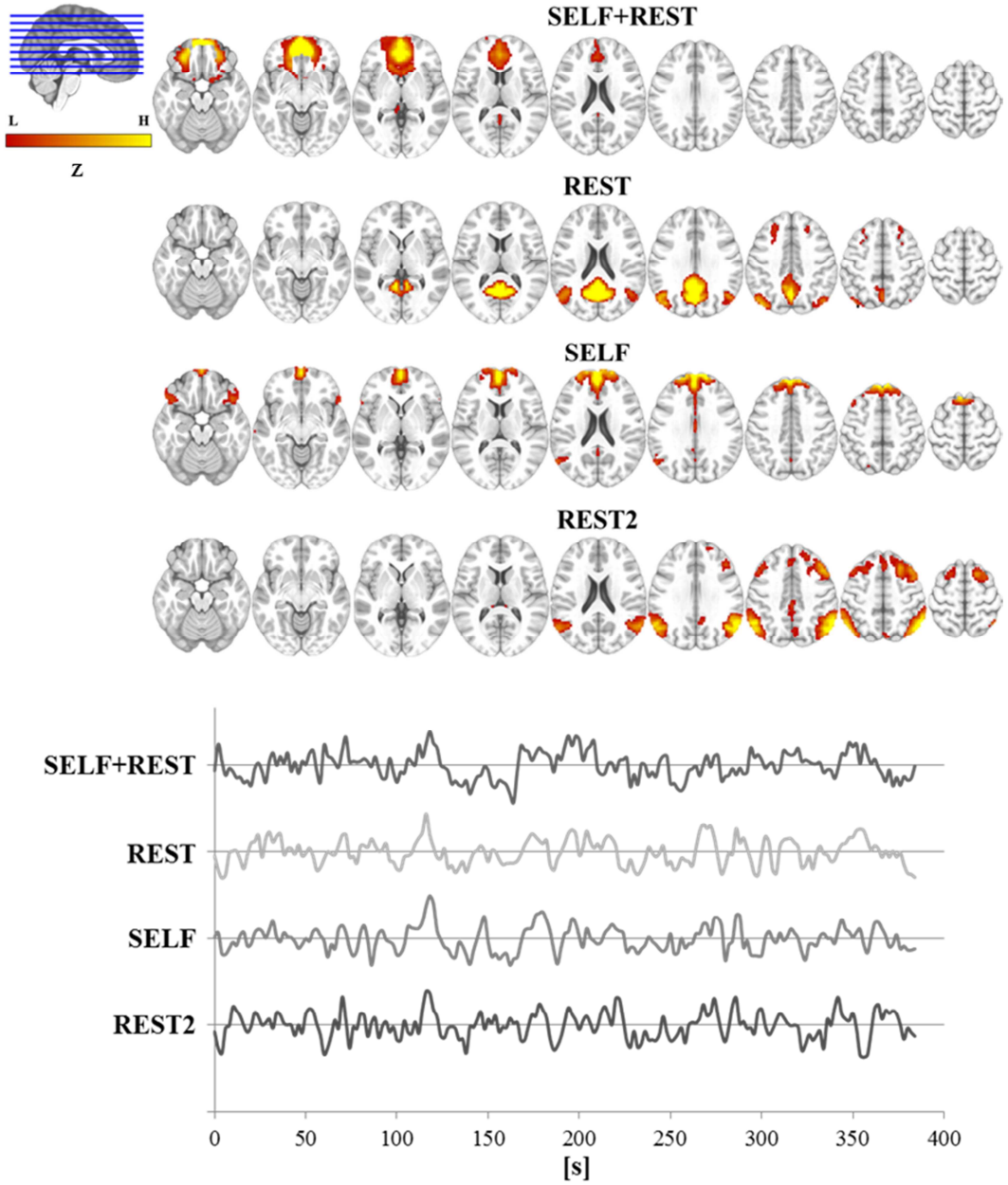

Figure 1.2: Axial spatial maps and related time courses of the resting state networks of interest reconstructed by group ICA. All spatial maps were converted to Z statistic images and thresholded at Z = 3.

As regards the spectral data, figure 1.3 illustrated the spatial distribution of the mean relative power of each band. As shown by the scalp topographies, relative power in delta band showed the lowest values over the midline and the highest values over the lateral scalp sites. Relative power in theta band had the smallest values over the centro-parietal electrodes and the biggest values over the lateral frontal electrodes. Relative power in alpha band was higher in the occipito-parietal

electrodes and lower in the fronto-temporal electrodes. The biggest values in beta band were localized over the central and the occipital electrodes. Concerning gamma band, the higher values were identified over mid lateralized central frontal electrodes.

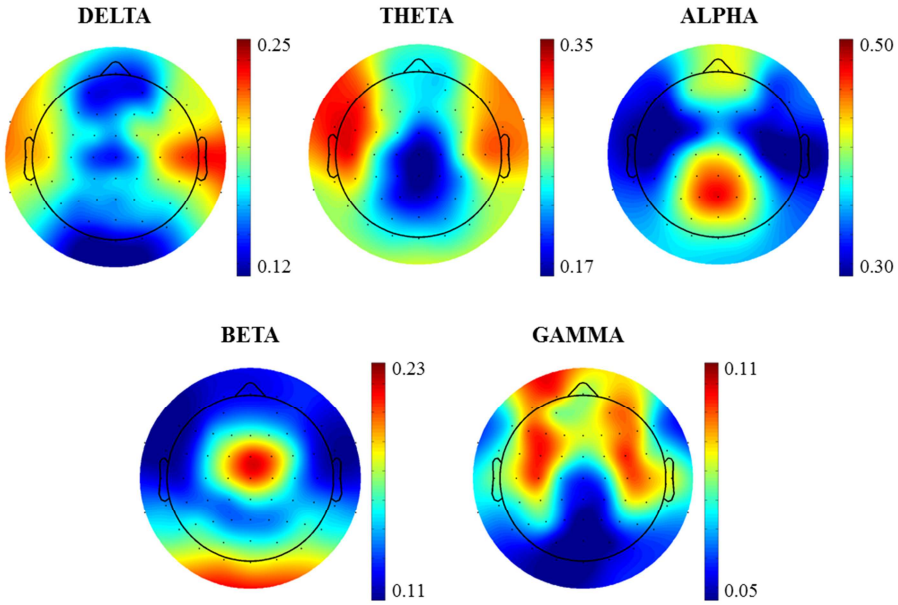

Figure 1.3: Spatial distribution over the scalp of the mean relative power across subjects in the delta (1-3.5 Hz), theta (4-7 Hz), alpha (7.5–12.5 Hz), beta (13–24 Hz) and gamma (24.5-45 Hz) bands. For each subject, the relative power in the bands of interest was computed in epochs of 2 s and then averaged. Each scalp topography was centred with respect to the minimal and maximal relative power of the electrodes. In this way, in all the topographical plot the minimal value is blue and maximal value is red (see the colour-scale on the right of each map).

1.8.2 Within network

Self+Rest

To infer how the time course of this RSN correlated with the different bands, five two-tailed one-sample t-tests were performed. Analyses revealed a number of statistically significant positive correlations with alpha, as well as negative correlations with theta (see figure 1.4). Scalp sites in the central-frontal region showed both positive correlation with alpha in Fz and F2 electrodes and negative correlation with theta in F1, Fz, F2 and FCz electrodes. In addition, significant positive correlations with alpha were distributed over the occipito-parietal electrodes with a clear right lateralization, whereas significant negative correlations were localized in the right occipito-parietal scalp sites.

Electrodes showing inter-band differences in the correlation with the fMRI signal were identified with ANOVA. Based on their topography, these significant band-dependent correlation differences were grouped into two distinct clusters (see Figure 1.4). The first cluster was located over central-frontal electrodes (FC1, F1-2, Fz). Post-hoc analyses on the electrode with the maximum effect (Fz) of the cluster revealed a significant difference in the mean EEG-fMRI correlations between alpha and theta bands (figure 1.4). The second cluster included electrodes over an extended bilateral occipito-temporo-parietal region, with a clear right lateralization of the magnitude of the effect. Post-hoc analyses on the electrode with the maximum effect (P6) revealed that mean network correlation with alpha band significantly differed from the correlation with other bands (figure 1.4).

Concerning correlations computed using complex measures derived from the ratios of different bands, results were shown in figure 1.4. In particular, significant negative correlation with beta/alpha ratio were found over the occipito-parietal electrodes (O1-2, Oz, PO8, P6) and significant positive correlations with alpha/theta ratio were found over Fz and F2 and over occipito-parietal electrodes with a right lateralization, mirroring the pattern of results observed in the analysis using the single bands (see above).

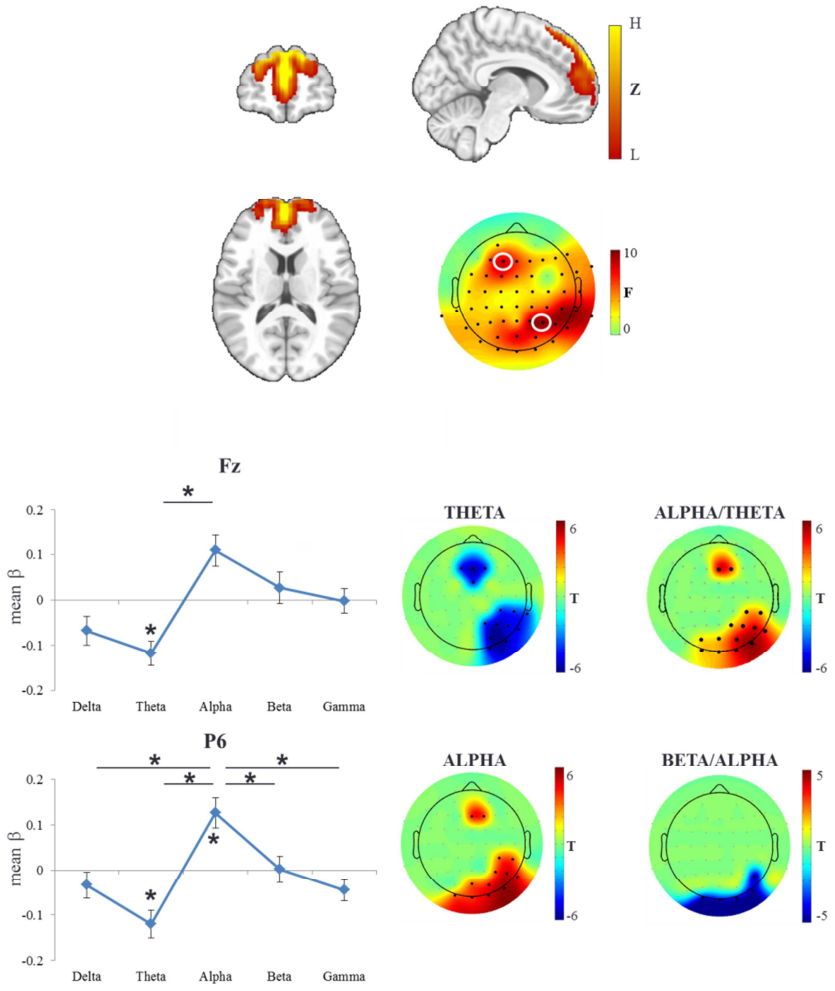

Figure 1.4: Results of the analysis aimed at investigating the spatial distribution of correlations between the activity of the "Self+Rest" network and the EEG rhythms. The figure shows the "Self+Rest" network by means of the three most informative orthogonal slices. The first scalp topography from top of the image illustrates the results of the ANOVA: electrodes in which a significant effect (TFCE corrected, $p < 0.05$) was found are indicated as black dots. White circles indicate the electrode with the maximal effect for each spatio-spectral cluster. For these electrodes, the across-subjects mean values of the correlations between the time course of the network and the different band power time series are plotted in the graphs on the left of the image. Black asterisks above or under the blue line indicate correlations between the activity of the network and the specific EEG rhythms that were significantly different from 0 (TFCE corrected, $p < 0.05$). Black asterisks over a black bar identify the significant results of the post-hoc tests (TFCE corrected, $p < 0.05$). On the right of the graphs, scalp topographies illustrate the bands in which significant correlations with the time course of the "Self+Rest" network were found; the significant electrodes are highlighted with black dots.

Rest

Electrodes in which the time course of the posterior regions of the Default Mode Network significantly covaried across subjects with the band-power time series were presented in figure 1.5. In particular, t-test analyses showed clusters of significant negative correlations with both delta and theta bands and positive correlations with alpha band. Negative correlations with delta were spread over the occipito-temporo-parietal sites, over the frontal electrodes and over the right central-frontal ones. In a spatially complementary cluster including central-frontal electrodes (C1, Cz, FC1 and FCz), negative correlations with theta were instead found. Finally, a cluster of electrode presenting significantly positive correlation with alpha were identified in the right temporal-parietal regions.

As shown in figure 1.5, ANOVA analysis revealed a significant modulation of EEG power-fMRI correlation across bands mainly in the posterior electrodes, with a right lateralization of the effect magnitude. The significant cluster also included temporal, left central-frontal and right frontal electrodes. The post-hoc test results for a frontal and a posterior representative electrodes (F1 and P6) are shown in figure 1.5. In details, analysis disclosed differences between alpha-fMRI correlations and delta- and theta-fMRI correlations in both the posterior and frontal electrodes. Other differences were found between delta and beta and between delta and gamma in the posterior and frontal electrodes, respectively.

Finally, significant positive correlations with alpha/theta ratio were identified in the central frontal electrodes (F1, FC1, FCz and Cz) and in the right parietal electrodes (P8, P6, P4, P2, TP8, CP6 and CP4) and illustrated in figure 1.5.

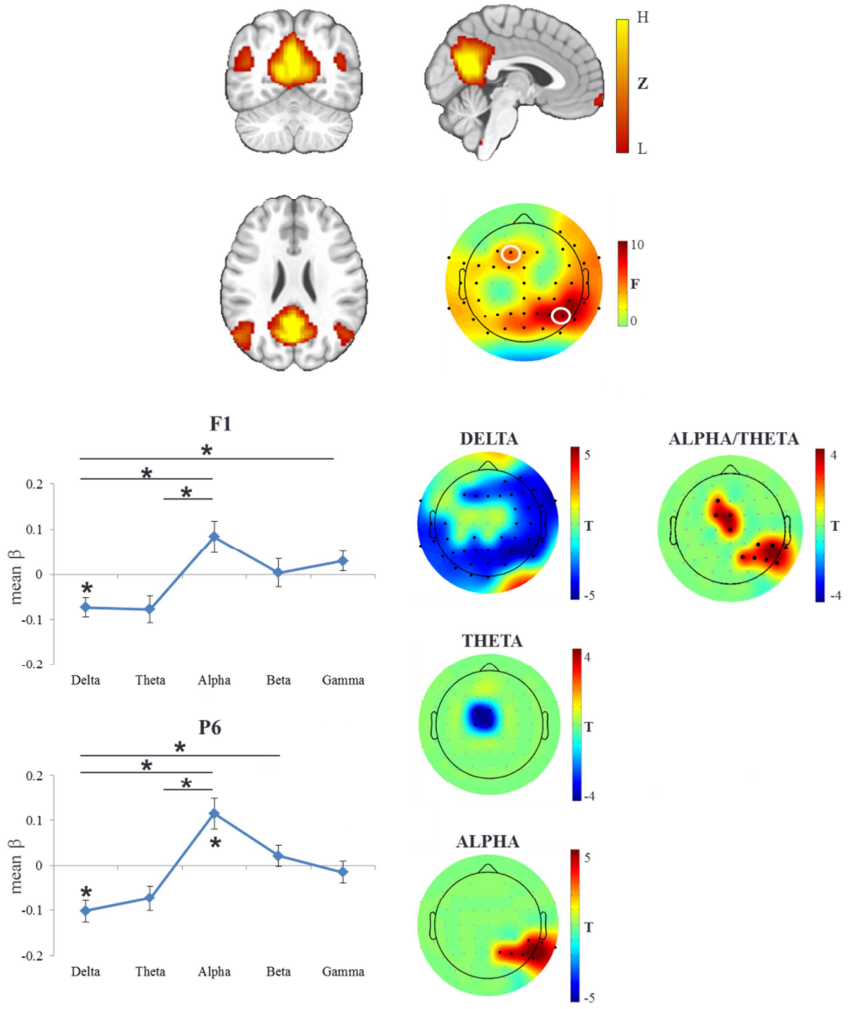

Figure 1.5: Results of the analysis aimed at investigating the spatial distribution of correlations between the activity of the "Rest" network and the EEG rhythms. The figure shows the "Rest" network by means of the three most informative orthogonal slices. The first scalp topography from top of the image illustrates the results of the ANOVA: electrodes in which a significant effect (TFCE corrected, $p < 0.05$) was found are indicated as black dots. White circles indicate the electrode with the maximal effect for each spatio-spectral cluster. For these electrodes, the across-subjects mean values of the correlations between the time course of the network and the different band power time series are plotted in the graphs on the left of the image. Black asterisks above or under the blue graph line indicate correlations between the activity of the network and the specific EEG rhythms that were significantly different from 0 (TFCE corrected, $p < 0.05$). Black asterisks over a black bar identify the significant results of the post-hoc tests (TFCE corrected, $p < 0.05$). On the right of the graphs, scalp topographies illustrate the bands in which significant correlations with the time course of the "Rest" network were found, the significant electrodes are highlighted with black dots.

Self

Tests for the statistical significance of the correlations between band power time series and the time courses of the network highlighted a number of significant negative correlations for delta and theta bands and positive correlations for alpha band, as shown in figure 1.6. Based on their spatial characteristics, correlations with delta time series were grouped in two clusters in the right part of the scalp. A smaller cluster was localized over the frontal and fronto-temporal electrodes (F6-8, FC6, FT8-10), whereas a bigger one was found over parietal and central-parietal electrodes. Correlations with theta band were widely distributed over occipito-parietal-temporal electrodes (with a right lateralization involving the temporo-parietal electrodes) and over bilateral fronto-central electrodes. Finally, correlations with alpha were observed over bilateral occipito-parietal electrodes (with a right lateralization concerning the effect magnitude), over right temporal and frontal electrodes and in a distinct left-lateralized cluster over central-frontal electrodes (F1-2, Fz, FC1-3).

Significant differences in the way the several bands correlated with the network BOLD signal were identified by means of ANOVA analysis over most of the scalp (see figure 1.6). Electrodes where the effect was maximal were localized in the left frontal region and in the right centro-temporo-parietal area. In these two subgroups, F1 and P4 electrodes were taken as representative to show the results of the post-hoc analysis. As presented in figure 1.6, significant differences in the EEG-fMRI correlations were found between delta and gamma, delta and alpha, theta and alpha, theta and beta both in the anterior and posterior areas. Other spatial-specific significant differences were also detected. Specifically, differences were shown over F1 electrode between delta and theta and over P4 electrode between theta and beta.

Significant correlations with alpha/theta ratio were also identified in a wide region of the scalp including frontal, central, parietal, occipital and right temporal scalp sites (figure 1.6).

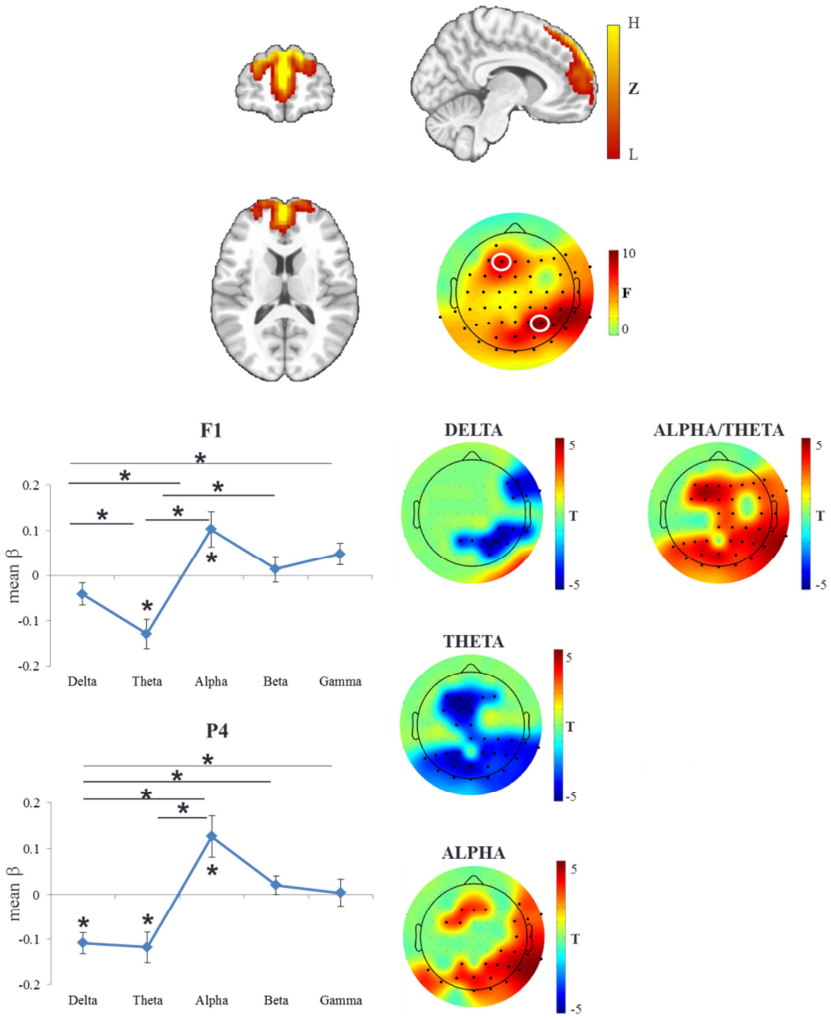

Figure 1.6: Results of the analysis aimed at investigating the spatial distribution of correlations between the activity of the "Self" network and the EEG rhythms. The figure shows the "Self" network by means of the three most informative orthogonal slices. The first scalp topography from top of the image illustrates the results of the ANOVA: electrodes in which a significant effect (TFCE corrected, $p < 0.05$) was found are indicated as black dots. White circles indicate the electrode with the maximal effect for each spatio-spectral cluster. For these electrodes, the across-subjects mean values of the correlations between the time course of the network and the different band power time series are plotted in the graphs on the left of the image. Black asterisks above or under the blue graph line indicate correlations between the activity of the network and the specific EEG rhythms that were significantly different from 0 (TFCE corrected, $p < 0.05$). Black asterisks over a black bar identify the significant results of the post-hoc tests (TFCE corrected, $p < 0.05$). On the right of the graphs, scalp topographies illustrate the bands in which significant correlations with the time course of the "Self" network were found, the significant electrodes are highlighted with black dots..

Rest2

As shown in figure 1.7, activity of the network significantly correlated with the slow EEG-derived time series mainly over the right posterior scalp electrodes. Specifically, significant negative correlations with delta and positive correlations with alpha were localized over a small cluster of parietal electrodes (CP2, P2-4 and P4-6, respectively). Significant correlations with theta covered a more extended region, including right centro-temporo-parietal electrodes and left central-frontal electrodes.

Significant modulations of EEG power-fMRI correlations across bands were found with ANOVA in a number of electrodes (see figure 1.7). Considering the topography and the strength of the effect, electrodes could be divided into two clusters: a smaller one with weaker effects over mid-left frontal electrodes (F1-FC1) and a more widespread one with stronger effects in the right centro-temporo-parietal electrodes. Significant differences in the way the band power time series were coupled with the BOLD signal were presented in figure 1.7 for the electrodes with the maximum F of the clusters. The ANOVA effects were explained by significant differences involving the alpha band as compared to theta, beta and gamma bands. Specifically, differences between alpha and theta correlations were found for both clusters, whereas differences between alpha and both delta and beta were only identified in the parietal cluster.

As regard the complex measures, figure 1.7 showed significant positive correlations with alpha/theta ratio over central-temporo-occipital electrodes.

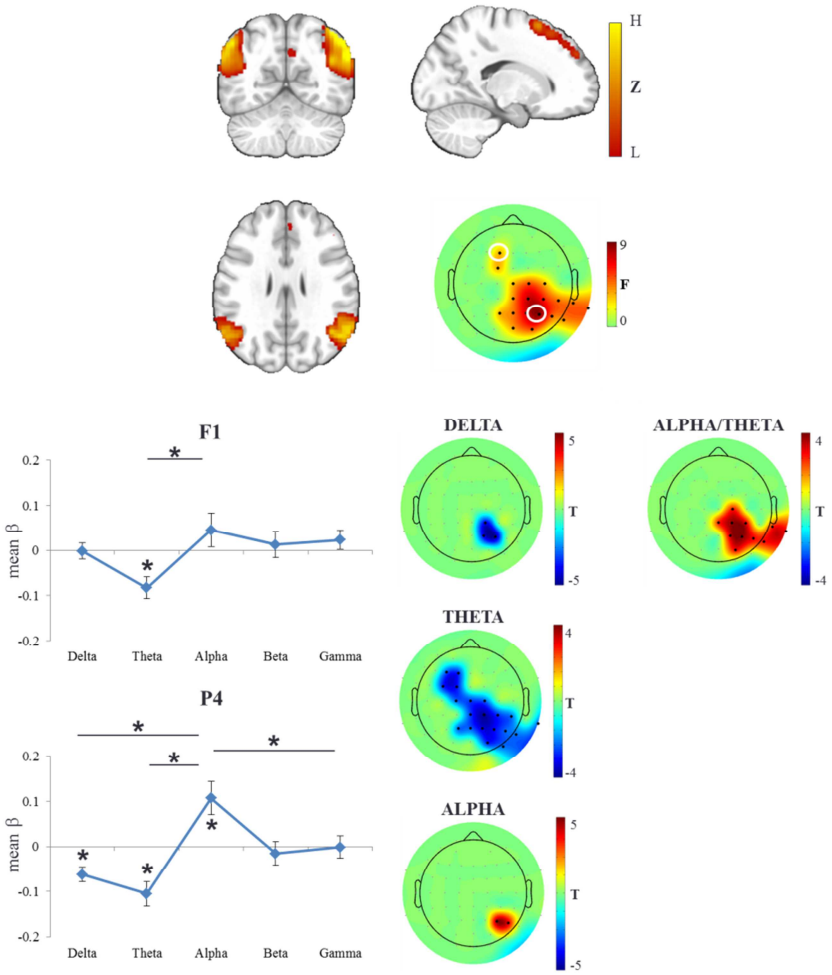

Figure 1.7: Results of the analysis aimed at investigating the spatial distribution of correlations between the activity of the "Rest2" network and the EEG rhythms. The figure shows the "Rest2" network by means of the three most informative orthogonal slices. The first scalp topography from top of the image illustrates the results of the ANOVA: electrodes in which a significant effect (TFCE corrected, $p < 0.05$) was found are indicated as black dots. White circles indicate the electrode with the maximal effect for each spatio-spectral cluster. For these electrodes, the across-subjects mean values of the correlations between the time course of the network and the different band power time series are plotted in the graphs on the left of the image. Black asterisks above or under the blue graph line indicate correlations between the activity of the network and the specific EEG rhythms that were significantly different from 0 (TFCE corrected, $p < 0.05$). Black asterisks over a black bar identify the significant results of the post-hoc tests (TFCE corrected, $p < 0.05$). On the right of the graphs, scalp topographies illustrate the bands in which significant correlations with the time course of the "Rest" network were found, the significant electrodes are highlighted with black dots.

1.8.3 Between networks

The results described above reflect the inter-band differences in the topographical distribution of EEG power-fMRI relationship for each subcomponent of the Default Mode Network taken separately. To find out whether these EEG-fMRI correlation patterns were component-specific or rather general features of the DMN, a mass univariate ANOVA in sensor x frequency space was performed with the four networks as a factor.

As shown in figure 1.8, the analysis revealed several spatio-spectral clusters of significant inter-networks differences in the EEG-fMRI correlations. A first cluster was visible over the occipital electrodes, which involved mainly theta and gamma bands; a second cluster was located over the right temporo-frontal electrodes and involved bands from delta to alpha; a third small cluster was present in the right parietal region of the scalp (CP6, P4-6) and involved the delta band; finally, a one-channel cluster was found over Cz for the theta band. Notably, concerning the spectral dimension, none of the clusters involved the high-frequency bands (beta and gamma bands). In figure 1.8, mean correlation between network fMRI signals and delta, theta and alpha bands, measured in a representative electrode of each spatio-spectral cluster, were plotted as function of the different networks. For the Oz electrode, located in the more widespread cluster, positive correlations with alpha as well as negative correlations with theta distinguished the two RSNs involved in self-related processes (Self+Rest and Self networks) from Rest and Rest2. In F2 electrode, belonging to the lateralized frontal cluster, positive correlation with alpha identified Self+Rest, Rest and Self networks with respect to Rest2, whereas negative correlation with theta discerned between the self-related and the rest-related subcomponents. In this scalp site, thus, each subcomponent of the DMN could be distinguished from the other ones, based on the combination of their correlation with alpha and theta bands. As regard the two minor clusters, in P6 electrode a negative correlation with delta band was specific of the Rest networks, whereas in Cz electrode a lack of negative correlation with theta band was characteristic of the Self+Rest subcomponent.

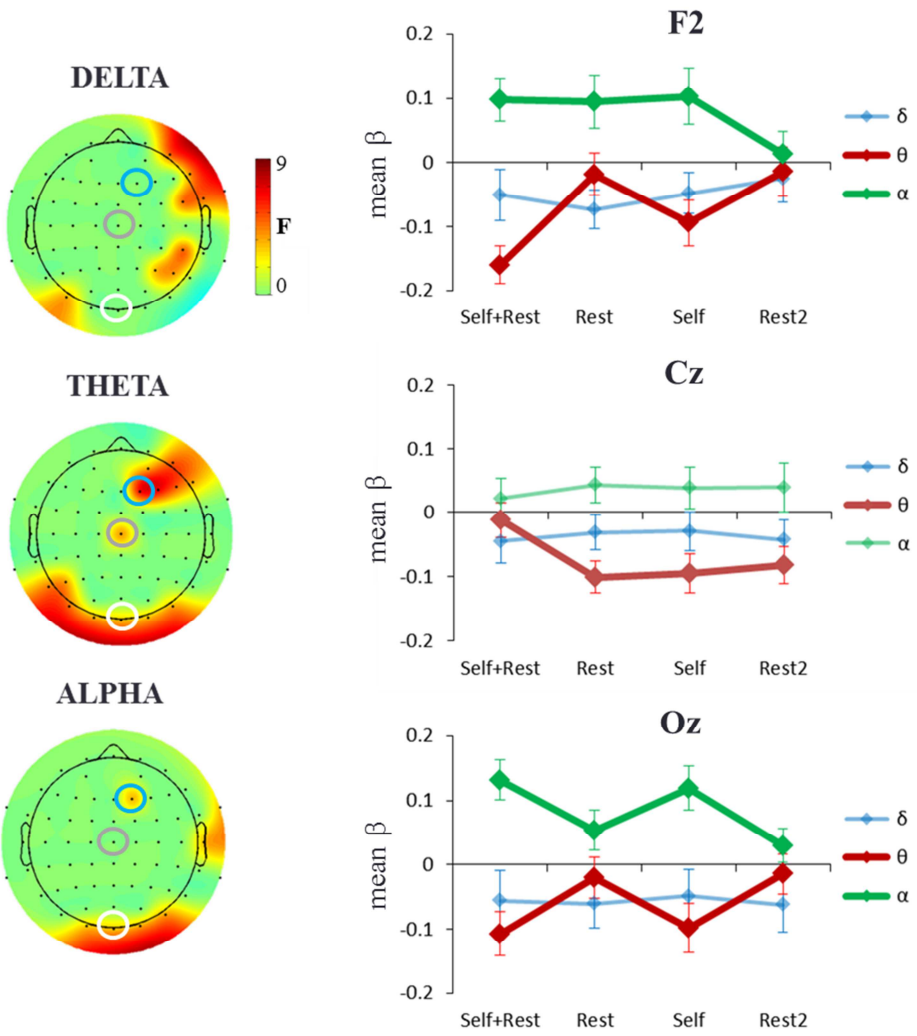

Figure 1.8: Results of the analysis aimed at investigating specific spatio-spectral patterns that were significantly different across the subcomponents of the Default Mode Network. Scalp topographies on the left of the image show the results of the ANOVA. On the right of the image, the across-subjects mean correlation between the networks and delta-, theta-, and alpha- band power time series in three electrodes are plotted. The three graphs refer to F2, Cz, and Oz, indicated in the scalp topographies with blue, grey, and white circles, respectively. In the graphs, the thicker lines represent bands for which the EEG-fMRI correlation significantly differed across networks. Beta and gamma bands are not presented because none of the clusters involved these bands.

1.9 Discussion

In the present study, an innovative and completely data-driven approach was used in order to investigate the scalp distribution of the patterns of correlations between, on the one side, the EEG spectral activity in the entire (i.e., 1-45 Hz) power spectrum and, on the other side, the low-frequency coherent fluctuations of the BOLD signal in different RSNs.

Concerning the EEG analysis, the scalp topographies of the mean relative power of each band presented here (see figure 1.3) revealed common band-dependent spatial distributions. For example, the spectral power in the alpha band was mainly distributed over the parieto-occipital scalp sites, while the power in the beta band has a more anterior distribution as compared to the alpha one. These results are thus consistent with the EEG scalp distributions previously reported in the literature (e.g.Michel et al. 1992) and indicate that the EEG preprocessing employed here was successful in reconstructing of the EEG data by eliminating the artifacts induced by simultaneous fMRI scanning.

As regards the fMRI BOLD data analysis, the hierarchical clustering analysis following the ICA identified a number of clusters, representing the different RSNs well established in the resting state fMRI literature using ICA, including a cluster of four sub-networks that, combined together, formed the (extended) default mode network (DMN). This finding is in line with previous studies showing that the DMN can be fractionated into distinct sub-networks based on their specific functional characteristics (Whitfield-Gabrieli et al. 2011, Andrews-Hanna et al. 2010). Specifically, it has been shown that there are associations and dissociations in cortical structures composing the DMN and either specifically related to self-referential thoughts and processes, such as the dorsal portion of the medial prefrontal cortex, or specifically related to “pure” (i.e., non self-referential) resting state, such as the precuneus and the angular gyri, or related to both mental states, such as the ventral portion of the medial prefrontal cortex (Whitfield-Gabrieli et al. 2011).

Given the mounting importance that the DMN has gained in current neuroscience research, we decided to apply our innovative analytical approach to the four sub-networks composing the DMN as an applicative proof of concept. The aim in making this choice was also to employ a conservative approach in verifying the validity and potential of the analytical approach used here in identifying even the supposedly more subtle differences exhibited by these four related sub-RSNs in their specific EEG-derived spatio-spectral fingerprints.

Generally, in line with a number of previous studies the RSN-specific results revealed that the four sub-networks of the DMN correlated positively with the alpha power over occipital channels (e.g., Jann et al. 2009, Jann et al. 2010, Mantini et al. 2007b) and negatively with theta power over frontal channels (e.g., Scheeringa et al. 2008, Mo et al. 2013, Jann et al. 2010). Moreover, despite these across-the-board correlations, this approach highlighted, for the first time, the presence of distinctive subcomponent-specific spatial-frequency patterns.

In conclusion, the present results confirm the idea that spontaneous brain activity during resting state can be characterized by a finite set of spatio-spectral patterns (Mantini et al. 2007b). More importantly, however, they also extend previous findings by identifying, for the first time, the specific scalp regions showing: 1) significant EEG-fMRI correlations within each specific band and (sub-)RSN, 2) significant inter-band differences in EEG-fMRI correlations within each-specific (sub-)RSN, and, importantly, 3) significant differences in patterns of EEG-fMRI correlations over different frequency bands across different (sub-)RSNs, representing specific spatio-spectral fingerprints of those RSNs. The present results thus suggest that the innovative analytical approach used in the present study can be fruitful in identifying the specific spatio-spectral fingerprints of the RSNs.

These results are useful to better understand the functional role of the low-frequency coherent fluctuations of the BOLD signal. Indeed, since EEG, contrarily to fMRI, is a direct measure of the neuronal activity, knowing which

electrophysiological rhythm is specifically related to a particular network provides new insights about the neuronal basis of the network function. This study therefore gives an important contribution to the identification of specific scalp distributions of the EEG-fMRI correlations (namely, regions of the scalp where the EEG-fMRI correlations are significant for a given network, or regions where pattern correlations are different among networks). It should still be noted that spatial resolution of the EEG signal is too low to infer about the location of the involved EEG sources. A further step forward could be thus to try extending the present findings in this direction by performing a source estimation study. However, it is currently not clear whether the EEG system we employed in the present study can provide adequate localization performance. For this reason, in order to assess the feasibility of future source estimation studies, an investigation of the source reconstruction accuracy with the EEG system used in the present study and the state-of-the-art techniques is needed. This issue is indeed the subject of the next study presented in this thesis.

2 Source Estimation Accuracy

2.1 The source estimation problem

As seen in the discussion of the previous chapter, the main limit of the EEG technique is its low spatial resolution, around 5 to 9 cm with the common EEG system (Nunez and Westdorp 1994, Babiloni et al. 2001). The EEG channels record electrical activities that are generated several centimetres below the scalp and that go through different resistive layers before being measured (Nunez and Westdorp 1994). These layers, especially the skull (Srinivasan et al. 1996), caused a blurring effect at the scalp level and so, the recorded activities are weighted sums of the underlying brain sources. Due to this volume-conduction-induced mixture, a given scalp topography could in principle have been generated by many different sources configuration. Therefore, a maximal activity over certain electrodes cannot be unequivocally attributes to the sources of the underlying area (Michel et al. 2004).

To overcome this limit, it is needed to solve the source reconstruction problem, that is, estimating the sources of the current inside the brain that most likely generated the voltage potentials measured on the scalp. It is well accepted that neuronal activity can be approximated by current dipoles (de Munck, van Dijk and Spekreijse 1988). To solve the source localization problem the first thing to do is computing the scalp potentials resulting from the current dipoles inside the head, the so-called forward problem. The next step consists to work back and in combination with the EEG data, calculate the sources that best fit the measure, the so-called inverse problem. The accuracy of the solution depends on several factors,

including the number and arrangement of the electrodes over the scalp, the approximation used to describe the head model and inverse solution method adopted (see for reviews Michel et al. 2004, Hallez et al. 2007, Grech et al. 2008).

In mathematical terms, solving the inverse problem means computing the potential $g(\boldsymbol{r},\boldsymbol{r}_{dip},\boldsymbol{d})$ generated by a dipole with dipole moment $\boldsymbol{d}$ (magnitude d and orientation $\boldsymbol{e}$) and position $\boldsymbol{r}_{dip}$, measured at a scalp site with position $\mathbf{r}$. That is, solving the Poisson's equation to obtain the potential V on the scalp due to the activity of the dipole inside the head. If there is more than one active source, the electrode potential can be expressed as follow:

$$m(\boldsymbol{r}) = \sum_i g(\boldsymbol{r}, \boldsymbol{r}_{dip_i}, \boldsymbol{d}_i) \tag{1}$$

and considering the superposition principle, it can be written as:

$$\sum_i g(\boldsymbol{r}, \boldsymbol{r}_{dip_i})\,(d_{ix}, d_{iy}, d_{iz})^T = \sum_i g(\boldsymbol{r}, \boldsymbol{r}_{dip_i})\,\boldsymbol{d}_i \boldsymbol{e}_i \tag{2}$$

where $\boldsymbol{d}_i = (d_{ix},d_{iy},d_{iz})$ is a vector of the three dipole magnitude components. For N electrodes and p dipoles:

$$m = \begin{bmatrix} m(\boldsymbol{r}_1) \\ \vdots \\ m(\boldsymbol{r}_N) \end{bmatrix} = \begin{bmatrix} g(\boldsymbol{r}_1,\boldsymbol{r}_{dip_i}) & \cdots & g(\boldsymbol{r}_1,\boldsymbol{r}_{dip_p}) \\ \vdots & \ddots & \vdots \\ g(\boldsymbol{r}_N,\boldsymbol{r}_{dip_i}) & \cdots & g(\boldsymbol{r}_N,\boldsymbol{r}_{dip_p}) \end{bmatrix} \begin{bmatrix} d_1\boldsymbol{e}_1 \\ \vdots \\ d_p\boldsymbol{e}_p \end{bmatrix} = \boldsymbol{G} \times \boldsymbol{D} \tag{3}$$

where $i = 1, \ldots, p$ and $j = 1, \ldots, N$.
Adding a noise matrix $\boldsymbol{n}$:

$$\boldsymbol{M} = \boldsymbol{G} \times \boldsymbol{D} + \boldsymbol{n} \tag{4}$$

where $\boldsymbol{M}$ is the matrix of EEG measures, $\boldsymbol{G}$ is the leadfield matrix describing the projection from each of p dipoles to each of N electrodes and $\boldsymbol{D}$ is the matrix of dipole moments. Matrix $\boldsymbol{G}$ is obtained solving the forward problem. Under this

formulation solving the inverse problem consists of estimate the matrix of the dipole moments $\widehat{\boldsymbol{D}}$ given the electrode positions and the EEG data $\boldsymbol{M}$, and the leadfield matrix $\boldsymbol{G}$ (Grech et al. 2008)**.**

The choice of which mathematical model to use depends on the number of dipoles considered and on the assumptions about their positions, orientations and magnitudes. The possible models presented in literature (see for review Grech et al. 2008) are: a single dipole having unknown time-varying magnitude, position, and orientation; a given number of dipoles with unknown time-varying magnitudes and unknown, but constant positions and orientations; a given number of dipoles with fixed known positions and unknown time-varying magnitudes and orientations; variable number of dipoles with a set of constraints on magnitudes, orientations and positions. The two main approaches to solve the inverse problem are the parametric and non-parametric methods. In the parametric methods, the model considers only few dipoles having unknown positions and orientations. With this assumptions solutions of the problem is non linear. On the other hand, non-parametric models (or Distributed Source Models) assume several dipole sources with fixed known locations (and usually fixed known orientations) in the whole brain or cortical grey matter and unknown magnitudes. In this case, since the dipole positions is already known the problem is linear. However, having $p \gg N$, the problem is ill-posed, that is, solution is non-unique and highly sensitive to small data variations.

As we can see later, in order to respond to the aim of our study, a non parametric method was used. So in the next lines, the bayesian framework from which this technique can be derived, will be introduced.

Bayesian formulation of the inverse problem

This technique aims to compute the solution $\hat{x}$ that maximizes the posterior distribution of x given the data y (Baillet and Garnero 1997). Solution can be written as:

$$\hat{x} = max_x[p(x|y)] \quad (5)$$

where $p(x|y)$ is the conditional probability density of x given the data y. According to Bayes'law:

$$p(x|y) = \frac{p(y|x)p(x)}{p(y)} \tag{6}$$

if the posterior density is assumed to have a Gaussian distribution, we find:

$$p(x|y) = \frac{p(y|x)p(x)}{p(y)} = \frac{exp[-F_\alpha(x)]/z}{p(y)} \tag{7}$$

where z is a normalization constant, $F_\alpha(x)=U_1(x)+\alpha L(x)$ where $U_1(x)$ and $L(x)$ are the energy function associated with $p(y|x)$ and $p(x)$, respectively, and $\alpha>0$ is the regularization parameter. So the solution $\hat{x}$ can be expressed as:

$$\hat{x} = min_x\big(F_\alpha(x)\big) \tag{8}$$

assuming the data noise to be white, Gaussian and with zero-mean, $U_1(x)$ can be written as:

$$U_1(x) = \|Kx - y\|^2 \tag{8}$$

where K represents here the forward solution and $\|.\|^2$ is the L_2 norm. It should be noted that $L(x)$ may be defined as a combination of spatial and temporal priors. Combining the previous equations:

$$\hat{x} = min_x\big(F_\alpha(x)\big) = min_x\big(\|kx - y\|^2 + \alpha L(x)\big) \tag{9}$$

Solution $\hat{x}$ is therefore a compromise between the fidelity to the data and the spatial/temporal smoothness based on the α value (Grech et al. 2008, Baillet and Garnero 1997, Gavit et al. 2001).

Concerning the source inverse problem, using the previous notation the current distribution estimate $\widehat{\boldsymbol{D}}$ can be compute as:

$$\widehat{\boldsymbol{D}} = \min\big(U(\boldsymbol{D})\big) \tag{10}$$

where:

$$U(\boldsymbol{D}) = \|\boldsymbol{M} - \boldsymbol{G}\boldsymbol{D}\|_R^{\,2} + \alpha L(\boldsymbol{D}) \tag{11}$$

The different methods belonging to Distributed Source Models class differed based on how L(**D**) is implemented.

2.2 Accuracy of the solution: the number of electrodes

EEG measures the surface electrical potential field generated by the neuronal activity. Obviously this field is continuous, but to be measured it is spatially sampled based on the electrode positions in the EEG montage. In accordance with Nyquist's theorem, sampling rate should be at least twice the highest frequency present in the signal. This statement can be applied in the temporal domain as well as in the spatial one. However, while antialiasing filters can be applied for temporal sampling, this is not possible for the spatial characteristics of the measure recorded over the scalp electrodes. Nonetheless , due to the fact that skull behaves as a low-pass filter of the electrical field (Srinivasan, Tucker and Murias 1998), theoretically, spatial sampling could be performed without risk of aliasing if a sufficient number of channels are used. For years, skull conductivity was assumed to be low (Rush and Driscoll 1968, Cohen and Cuffin 1983), so measuring the electric field in a small number of positions did not seem a problem. However, more recent studies (e.g., Zhang, van Drongelen and He 2006b, Oostendorp, Delbeke and Stegeman 2000) have revealed that skull conductive was higher and, therefore, an increase of the sampling density has become necessary. Freeman and colleagues (2003) suggested an optimal electrodes distance of 1 cm, implicating

that around 500 channels should be used (Song et al. 2015). Considering that, in the clinical environment 32 channels or less are usually employed, whereas in the research 64- and 128- channel montages are the most widely used, spatial sampling presently used may be sub-optimal.

Several studies (e.g., Laarne et al. 2000, Lantz et al. 2003) dealt with the defining of a minimum number of electrodes to avoid poor performance. Laarne et al. (2000) examined the relationship between the number of electrodes and dipole localization accuracy using a realistic head model and simulated data. In particular, they considered two different montages with 19 and 58 channels and 45 cortical source locations, to which random noise were added. In the forward model, computed using finite difference method (FEM), they took into account scalp, skull, cerebrospinal fluid, grey matter and white matter. Dipoles localizations were estimated with a least square algorithm and for two different values of the skull resistivity. They found that, by increasing the number of the electrodes, localization accuracy improved in the presence of noise. The first study in which the performances of EEG source localization results were estimated for montages with more than 100 electrodes was reported in a study by Lantz et al. (2003). They compared the accuracy of source localization with nine different electrodes configuration, from 25 to 166 channels, using epileptiform activity and simulated data. Forward model was solved based on a three-shell spherical head model for simulated data and on an anatomically-constrained spherical head model for the clinical data. They estimated the inverse problem by using EPIFOCUS (Grave de Peralta Menendez et al. 2001, Lantz et al. 2001) and found that, in general, precision on source localization did not exhibit a linear relationship with the number of electrodes. Specifically, the bigger improvement was seen from 31 to 63 channels, whereas around 100 electrodes, the pattern reached a plateau. These results were in line with the general suggestion of a 3 cm inter-electrode spacing, achievable with about 100 electrodes (Michel et al. 2004, Plummer, Harvey and Cook 2008). Also Wang et al. (2011) and Lu et al. (2012) observed better performance using a higher number of electrodes, but in both studies the performances were analysed until 76 electrodes montages.

A more extended analysis was recently reported by Sohrabpour and colleagues (2015). Specifically, in their study, they investigated the mean localization errors when source estimations were computed on 32, 64, 96 and 128 electrodes montage. Assessments were conducted on epileptic paediatric patients and on synthetic data with various SNR values (10, 7, 3, 0 dB). As regard simulated data, dipoles were located in 100 points with random position and orientation and performances were averaged across them. They used three layer boundary element method (BEM) describing scalp, skull and brain to build the head model and calculated the distributed dipole inverse solution with sLORETA (Pascual-Marqui 2002). Authors found that localization improvement rate decreased with increasing number of electrodes both in patient's data and simulations. In particular synthetic data showed this pattern regardless of noise level. To statistically analyse the general impact of different electrode configurations on localization errors, they also performed paired t-test between any pair of electrode configurations and found that all the comparisons were significant. These results were then replicated by Song et al. (2015), who compared the accuracy on source reconstruction as a function of the channels density and coverage of the inferior and superior head regions. They conducted the analysis both on simulated data, to which 10 SNR Gaussian noise were added, and epileptform EEG data. Solutions were computed with Minimum Norm (MN) (Dale and Sereno 1993) and sLORETA (Pascual-Marqui 2002) based on a realistic head model describing scalp, bone, cerebral spinal fluid, white matter, grey matter, air compartments and eyeballs. They found that in general sLORETA and the whole-head coverage allowed to achieve better performance in terms of mean localization errors across brain sources (2447 dipoles in the simulated data, 2000 dipoles in the patient's data). More, by comparing the performance obtained with 32, 64, 128 and 256 channels montages, they reported that localization was accurate when using 128 electrodes and that only slight increases were observed with a 256 channels montage.

2.3 Aim of the study

All the above-mentioned studies reported the mean localization errors across brain, and regional performances were only evaluated with clinical data, where epileptic seizure happened, often the temporal lobe (Lantz et al. 2003, Sohrabpour et al. 2015, Song et al. 2015). To our knowledge, no study has yet investigated the accuracy of source localization throughout the whole brain, depending on EEG sensors density. In this study, in order to overcome the limit of previous studies consisting in assessing the performances based on the mean values, 20 simulations for 32-, 64-, 128- and 256- channels EEG montages were performed. In this way, a statistical comparison between electrodes configuration at the voxel level became possible.

Briefly, based on the structural magnetic resonance imaging of the Colin template a realistic head model was built. The EEG montages were registered to the scalp and the locations of dipoles (i.e., brain sources) were arranged in a grid covering the grey matter. For each montage, the scalp potentials generated by the activity of each source were calculated. This source localization technique was applied to the simulated potentials and performances of reconstruction were quantified by means Localization Error and Spatial Spread.

Although 32-channels and 256-channels configuration are not widely used because of their bad performance and high cost, respectively, they were considered as the extremes to which compare performance of 64-channels and 128-channels.

The analyses were performed using NET Software, courteously provided by BIND group (http://www.bindgroup.eu/), and Matlab R2016b (The MathWorks, Natick, 2016), according to each specific preprocessing step.

2.4 EEG electrode montages

Electrode positions of the 256-channel montage were obtained from the 256-channel HydroCel Geodesic Sensor Net (Electrical Geodesics, EGI, Eugene, OR). Then, the 128-, 64-, and 32- channel positions were derived, as follows: the corresponding standard EEG montages derived from the extended 10-20 system were coregistered to the 256-channel montage and, for each of these three montages, the position of each channel in the standard configuration was replaced by the closest position in the 256-channel configuration. The sensor positions of each montage are shown in figure 2.1.

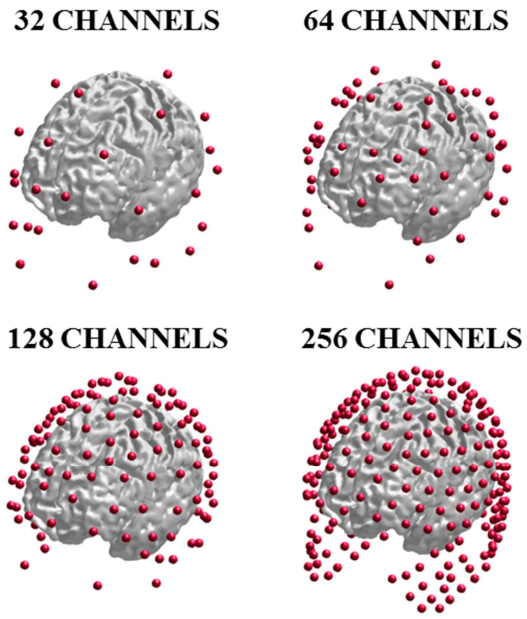

Figure 2.1: Position of the electrodes in the 32-, 64-, 128-, and 256-channel EEG montages.

2.5 Generation of simulated data

The generation of simulated EEG scalp potentials, obtained from the activity of a brain source, requires the head model estimation and the definition of the electrode positions in the same coordinate system as the structural image.

First, the volume conductor model was derived from a "representative" individual, Colin27 (http://www.bic.mni.mcgill.ca/ServicesAtlases/Colin27) (Holmes et al. 1998). This image was already matched to the MNI305 atlas, the Montreal Neurological Institute's 305-subject average MRI (http://imaging.mrc-cbu.cam.ac.uk/imaging/MniTalairach). For the head model, the description of the different head tissue types, each with a specific conductivity value, was needed. Typically, only scalp, skull, cerebrospinal fluid and brain (possibly separated into white and grey matter) are distinguished. They can be represented with a set of concentric spherical shells (e.g.,Vatta, Bruno and Inchingolo 2005) or incorporated in a realistic geometric model of the head (e.g., Fuchs, Wagner and Kastner 2001, Zhang et al. 2006a) .The latter approach has been shown to significantly improve the source localization (Vatta et al. 2010), therefore it was chosen. Moreover, in line with Liu and colleagues (2017), a realistic head model taking into account 12 tissue classes (skin, compact bone, spongy bone, cerebrospinal fluid, cortical grey matter, cerebellar grey matter, cortical white matter, cerebellar white matter, brainstem, eyes, muscle and fat) was used (see figure 2.2 for the details of the segmentation). The spatial resolution of the Colin structural image (voxel size: 1 × 1 × 1 mm) was not enough to directly identify all the tissues in it, so the template, where the segmentation was defined, was coregistered to the structural image with NET software. Twelve-tissue segmented image was obtained from (www.itis.ethz.ch/virtual-population/regional-human-models/mida-model/mida-v1-0) (Iacono et al. 2015) and the conductivity values, listed in table 3.1, were taken from literature (Haueisen et al. 1997).

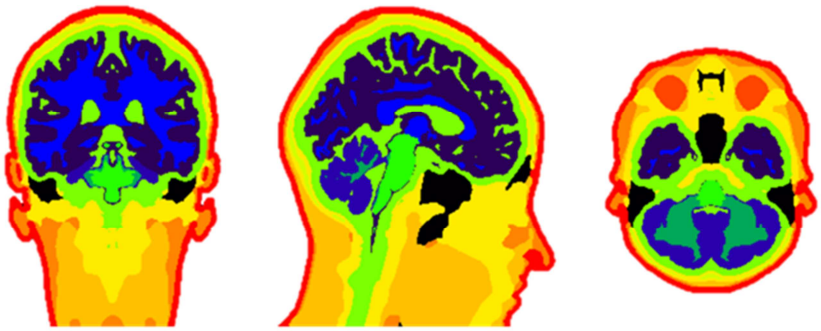

Figure 2.2: Result of the segmentation of the anatomical image of the template.

Tissue	Conductivity (S/m)
Skin	0.4348
Compact bone	0.0063
Spongy bone	0.0400
CSF	15.3850
Cortical gray matter	0.3333
Cerebellar gray matter	0.2564
Cortical white matter	0.1429
Cerebellar white matter	0.1099
Brainstem	0.1538
Eyes	0.5000
Muscle	0.1000
Fat	0.0400

Table 2.1: Conductivity values of the different tissues considered in the head model construction. Values were taken from literature (Haueisen et al. 1997).

To align the EEG electrodes to MR space the procedure described in the study by Liu et al. (2017) and implement in the NET software was adopted. First of all, based on three anatomical landmarks (nasion, left and right preauricular, MNI coordinates [0, 85,-30], [–86, 16, 40], and [86, 16, 40]), whose positions were known in both reference systems (EEG and MR), a rigid-body transformation was estimated and then applied to the electrode positions. This step alone did not guarantee their correct arrangement, since some of them might have been turned up inside the head. The issue was fixed using the Iterative Closest Point (ICP) registration algorithm (Besl and McKay 1992), with the head surface, derived from the structural image, considered as target. In a further step, each electrode position was then projected onto the closest head surface point.

A leadfield matrix, which describes the scalp electric potential generated by each source, was computed using the Simbio FEM method as implemented in FieldTrip toolbox (http://www.fieldtriptoolbox.org). To do this, geometric and electric properties of the head model have to be represented with a mesh. So, from the

coregistered template a regular hexahedral mesh (the points of the mesh are connected in such way that they create hexahedrons) was estimated for each of the 12 tissue types. Hexahedral mesh was chosen as a good compromise between a fast model construction process and good accuracy (Rullmann et al. 2009).

Since we are interested in assessing the performance of source reconstruction in all the possible positions of the sources, locations of the dipoles, corresponding to brain sources, were derived by discretizing the grey matter with a regular 3 mm grid. This resulted in 408,858 dipoles (namely, 136,286 dipole locations with *x, y* and *z* orthogonal directions).

The simulated EEG potentials were obtained by forward projection of each dipole to scalp sensors using the leadfield matrix, equation 4. A Gaussian white noise realization was added to each scalp topography in order to achieve a SNR (signal-to-noise-ratio) equal to 10 (Song et al. 2015, Pascual-Marqui et al. 2011). SNR was here calculated as the ratio between variance of the signal and variance of the noise.

The aforementioned steps (except for procedures related to image segmentation) were performed for each montage, and 80 simulated dataset (20 for each electrode configuration) were generated.

2.6 Source Localization

Inverse problem was solved with a Distributed Source Model, specifically with the exact low resolution brain electromagnetic topography algorithm (eLORETA) (Pascual-Marqui et al. 2011), as implemented in Fieldtrip. The primary feature of this method is that it has been shown to have zero localization error when tested with point-sources anywhere in the brain, under noise-free conditions. Going back to equation 10-11, the formulation of the problem can be stated as follow:

$$\widehat{D} = arg\,min_D\ \{\|M - GD\|^2 + \alpha D^T W D\} \quad (12)$$

where $\alpha > 0$ is the Tikhonov regularization parameter, which represents the relative weight between the data fitting error and the spatial smoothness constraint, and $W \epsilon \mathbb{R}^{p \times p}$ is a symmetric positive definite weight matrix. The solution of this problem is:

$$D = W^{-1}G^T\,(GW^{-1}G^T + \alpha H)^+ M \quad (13)$$

where the superscript $+$ denotes the Moore-Pensore pseudoinverse operator (which is equal to the inverse operator if the matrix is non-singular), and $H \epsilon \mathbb{R}^{N \times N}$ is the average reference operator. In eLORETA, weights are obtained from the following non-linear system of equations:

$$w_i = \left[{G_i}^T (GW^{-1}G^T + \alpha H)^+ G_i\right]^{1/2} \quad (14)$$

where w_i, for $i = 1, \ldots, p$, are the elements of the diagonal weight matrix W, and $G_i \epsilon \mathbb{R}^{N \times 1}$ indicates the ith column of the leadfield matrix G.

By solving the inverse problem (see equations 12-14), the contribution of each source along *x*, *y*, and *z* directions (D_x, D_y, D_z, respectively) were obtained for each scalp topography. Electrical activity of each dipole was then computed by the formula:

$$F = \sqrt{{D_x}^2 + {D_y}^2 + {D_z}^2} \quad (15)$$

2.7 Assessment of source localization accuracy

Simulated data consisted of 408,858 forward projections of each dipole with known location and orientation to scalp electrodes (*x*, *y*, *z* directions at 136,286 locations). Therefore, performance of source localization could be quantified for each dipole by means of Localization Error (LE) and Spatial Spread (SS) (Hauk, Wakeman and Henson 2011, Song et al. 2015, Molins et al. 2008). Localization Error (equation 6) is the Euclidean distance between the inverse solution's peak and the true location of the generating source, whereas Spatial Spread (equation 7) is a measure of the width of the distribution around the true source location. In the best scenario, both LE and SS should have small value. For a given dipole j, LE and SS can be estimated with the following formulae:

$$LE_j = \left\| x_j - x_{max} \right\| \tag{6}$$

where x_j is the coordinate of the true source and x_p is the coordinate of the dipole with the maximum power.

$$SS_j = \sqrt{\sum_i d_{ij} {F_{ij}}^2 \Big/ \sum_i {F_{ij}}^2} \tag{7}$$

where F_{ij} is the electrical activity measured at the position of the dipole i when the dipole j is active and d_{ij} is the Euclidean distance between dipole i and j.

Metrics were computed for all the 408,858 forward projection. For a given metric, three values were assigned to each dipole, corresponding to the accuracy of the estimation depending on its orientation. Potential differences along *x*, *y*, and *z* were evaluated by means of mass-univariate analysis (ANOVA) with the three orientations as factor. Since no significant effect of orientation emerged for any electrodes configurations (FDR corrected, $p < 0.05$), metrics were averaged across the orientations. Brain regions in which an increase of the spatial sampling density

(i.e., a higher number of electrodes) was related to a better performance were identified by means of right tailed Wilcoxon ranksum test (FDR corrected, $p<0.05$).

2.8 Results

2.8.1 Localization Error

The violin plots in Figure 2.3 showed, for each electrodes montage, the distribution of localization errors averaged across simulations and directions. For 32, 64, 128 and 256 channels, median LE (interquantile range, iqr) were respectively 2.20 (iqr = 1.60), 1.26 (iqr = 1.26), 0.84 (iqr = 1.1) and 0.53 (iqr = 0.52) cm.

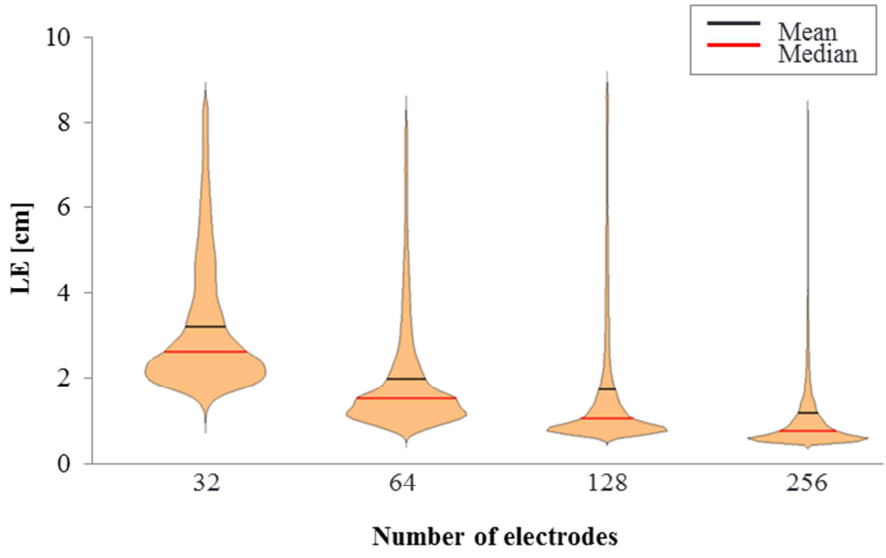

Figure 2.3: Violin plots showing the distribution of LE values as a function of the number of electrodes of the EEG montages. For each montage, LE values were averaged across x, y, and z directions and across the 20 simulations.

This metric exhibited a non-linear decay as a function of number of channels N_e; specifically, as shown in figure 2.4, it followed the power function

($LE_{median}(N_e) = 25.45 \times {N_e}^{-0.71}$, $R^2 = 0.995$), approaching zero as the number of channels increased.

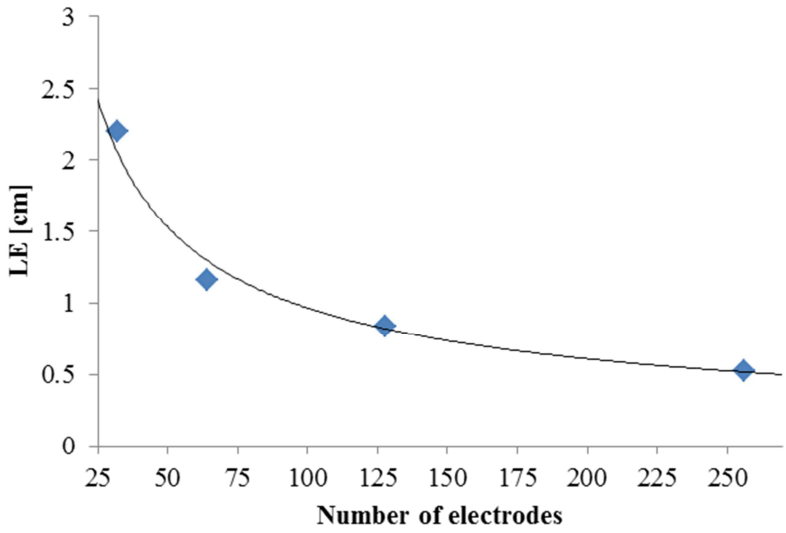

Figure 2.4: Graph showing the median of LE values as a function of the number of the electrodes of the EEG montage. Values (blue diamonds) were fitted with a power function (black line).

To evaluate the performance in estimating superficial and deep sources, LE for a given source position was plotted in figure 2.5 as a function of the distance of that source from the centre of the head (the lower the distance value, the deeper the source position).

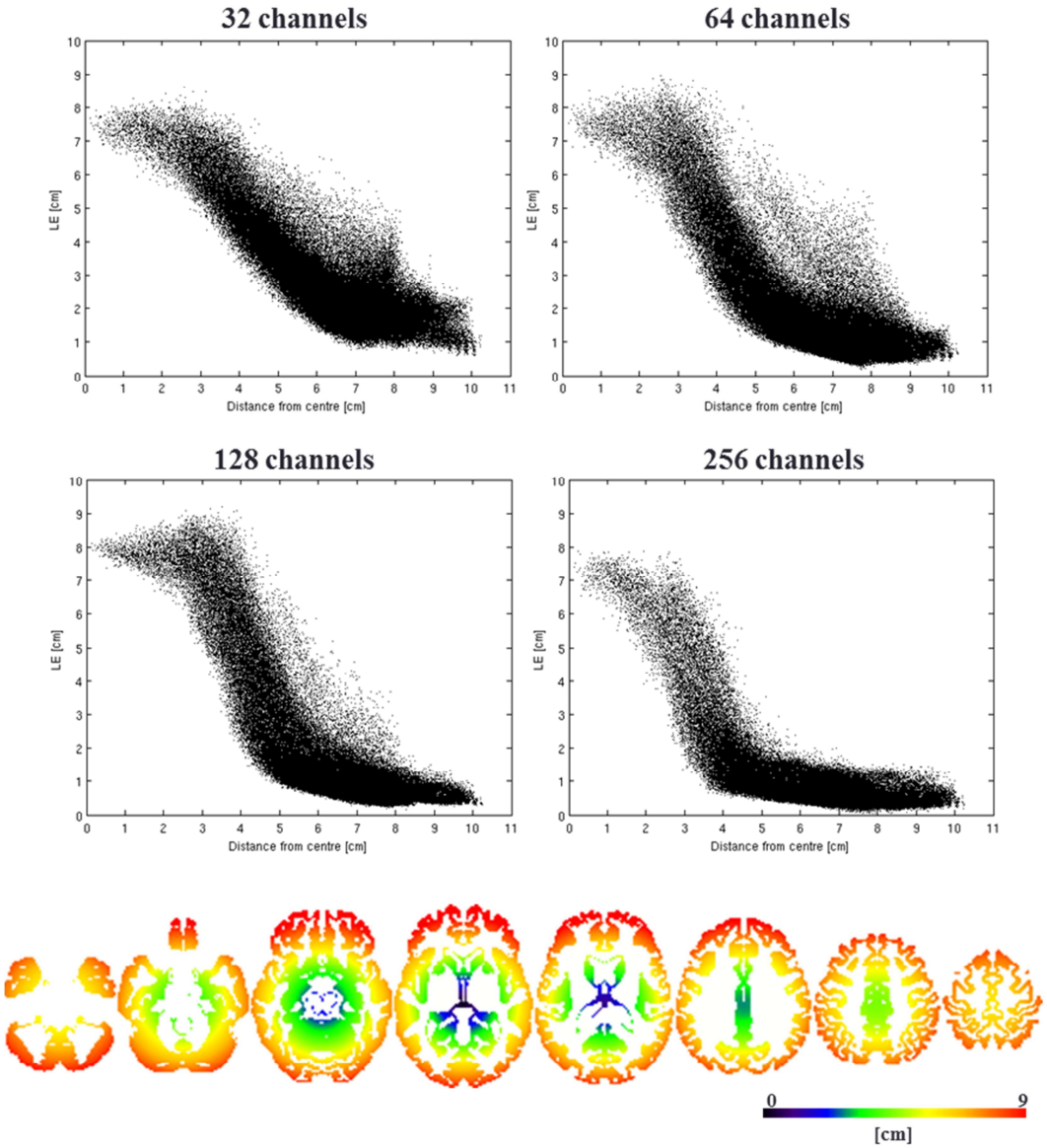

Figure 2.5: Graphs showing, for each EEG montage, the corresponding LE values as a function of the distance of the dipoles from the centre of the head. Last row shows in a color-scale the distance with respect of the centre of the head of each dipole position (see colorbar in the bottom right corner of the figure).

It can be seen that, independently from the sampling density of the montage, there was a monotonic decrease of LEs with increasing distances. It is interesting to note that the shapes of these relations can be fitted by sigmoid functions. To further assess the impact of source depth on LEs, the brain distribution of LEs was evaluated (see figure 2.6). All the configurations showed radials patterns of LEs, with the highest values in the subcortical structures and the lowest ones in the more superficial areas. By reading the figure by column, it can be seen that LE values decreased as a function of the number of the electrodes, although the spatial

patterns remained the same. Considering for instance the sources in the insula, errors committed in the estimation of their position were around 4 cm with a 32 channels montage (red colour), but decreased with 64 and 128 electrodes (green colour) up to reach values around 1 cm (blue colour) when using 256 channels.

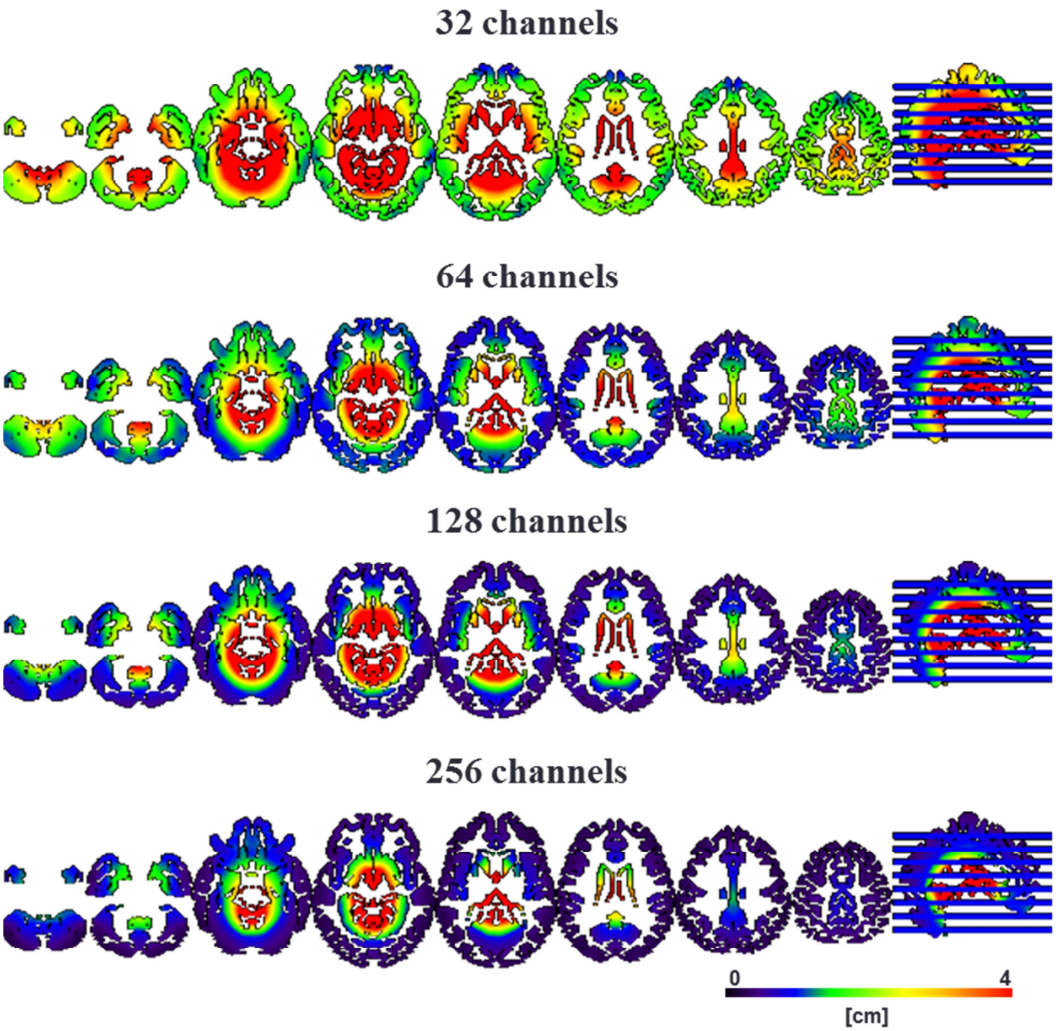

Figure 2.6: Spatial maps showing, in a color-scale, the brain distribution of LE values for each EEG montage (see colorbar in the bottom right corner of the figure).

The tests to assess if the localization errors significantly decrease across montages (Wilcoxon ranksum test) revealed that, when using 64 channels, error significantly decreased in all positions with respect to 32 channels. Moreover, significant improvements were also found switching from the 64-channel montage to the 128-channel one. However, as shown in figure 2.7, the deepest structures and some

cortical regions within the superior frontal gyrus, the supramarginal gyrus, the angular gyrus, the primary motor cortex and the lateral prefrontal cortex yielded comparable results; in other words, the localization of sources in these regions did not significantly improved when using 128 channels instead of 64 channels. Finally, with 256 channels the improvement was remarkable in the whole brain with respect to 128 channels.

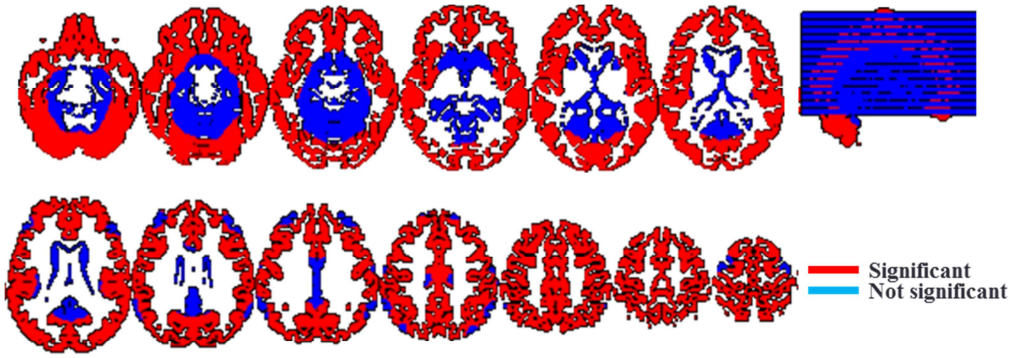

Figure 2.7: Spatial map showing the results of the Wilcoxon runksum test between LE values of the 64- and 128-channel montages. Blue color indicates the cortical regions in which LE values did not significantly decrease moving from the 64-channel to 128-channel montage.

To evaluate whether the performance for a given dipole position could depend on how much that position was close to all the electrodes, for each montage, the median distance of all the dipoles to all the electrodes was computed. In figure 2.8, LEs were plotted as function of this measure (right panel); at the left of each plot, the measure profile of the corresponding configuration was portrayed. As can be seen, the spatial pattern was different across montages due to their differences in the scalp distribution and density of channels. In all montages, although with different patterns, LE decreased in a non-linear way with increasing distances.

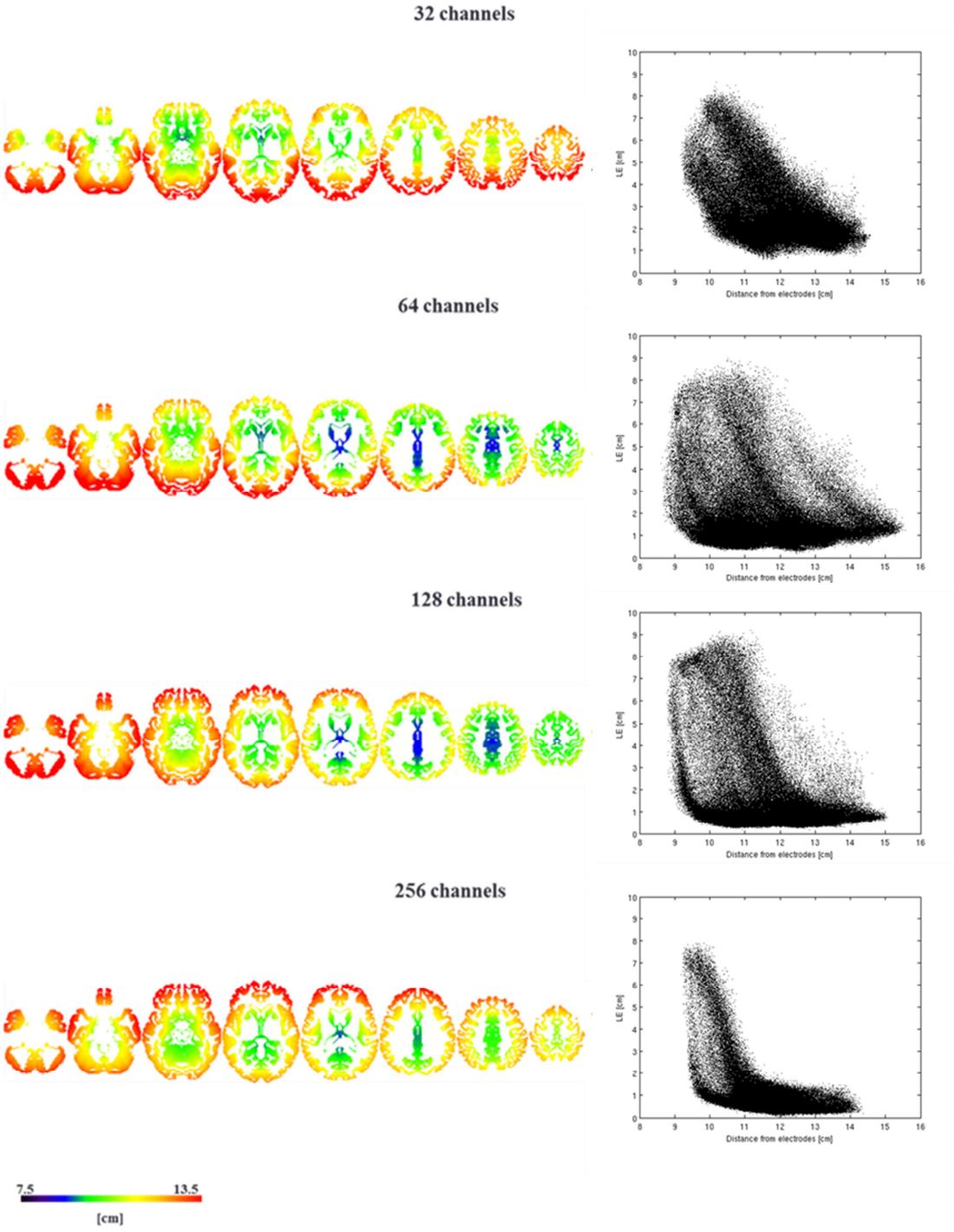

Figure 2.8: The right column of the figure shows for each EEG montage, the corresponding LE values as a function of the dipoles median distance from all the electrodes (Distance from electrodes). The left column shows, for each montage, the brain distribution of the "Distance from electrode" measure (colorbar illustrated on the bottom left of the figure). Note that spatial profile changes with the EEG montage.

2.8.2 Spatial Spread

In figure 2.9, the violin plots of average spatial spread across simulations and directions were presented for each channels configuration. For 32, 64, 128 and 256 electrodes, median SS were respectively 2.35 (iqr = 0.08), 2.16 (iqr = 0.13), 2.10 (iqr = 0.18) and 1.97 (iqr = 0.22) cm. As for LE, SS exponentially decreased as a function of the number of channels N_e, ($SS_{median}(N_e) = 3.09 \times {N_e}^{-0.08}$, R^2 = 0.966), see figure 2.10.

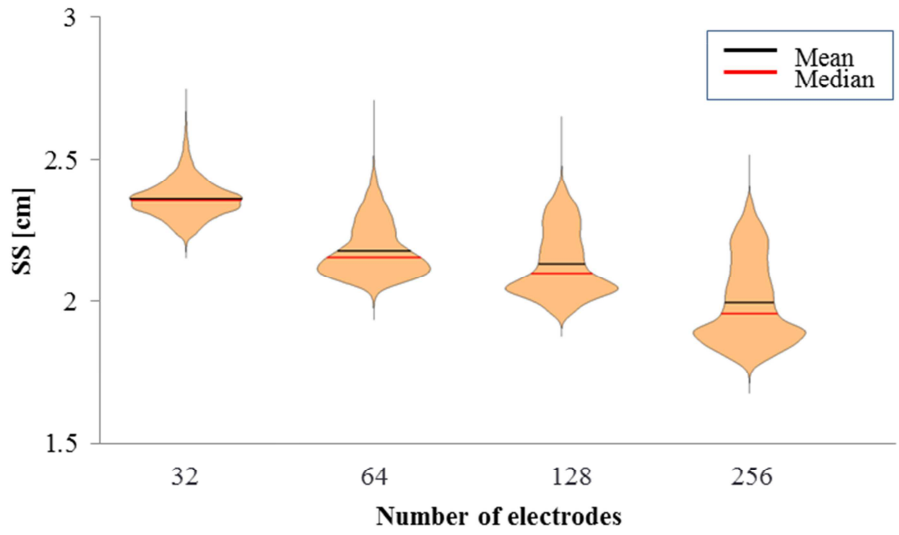

Figure 2.9: Violin plots showing the distribution of SS values as a function of the number of electrodes of the EEG montages. For each montage, SS values were averaged across x, y, and z directions and across the 20 simulations.

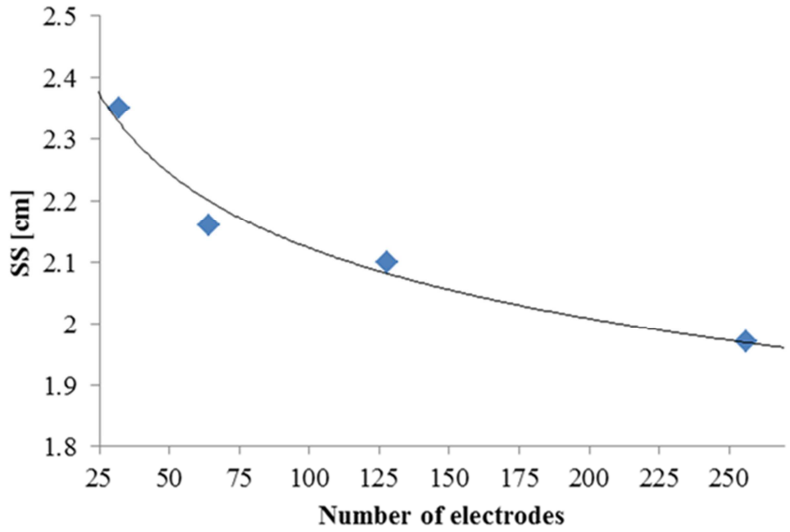

Figure 2.10: Graph showing the median of SS values as a function of the number of the electrodes of the EEG montage. Values (blue diamonds) are fitted with a power function (black line).

In figure 2.11, SS was plotted as a function of the dipole's distance from the centre of the head separately for each montage. Despite the presence of non-coherent sub-samples of data points, data seemed to follow a sigmoid function, especially for montages with 64, 128 and 256 electrodes.

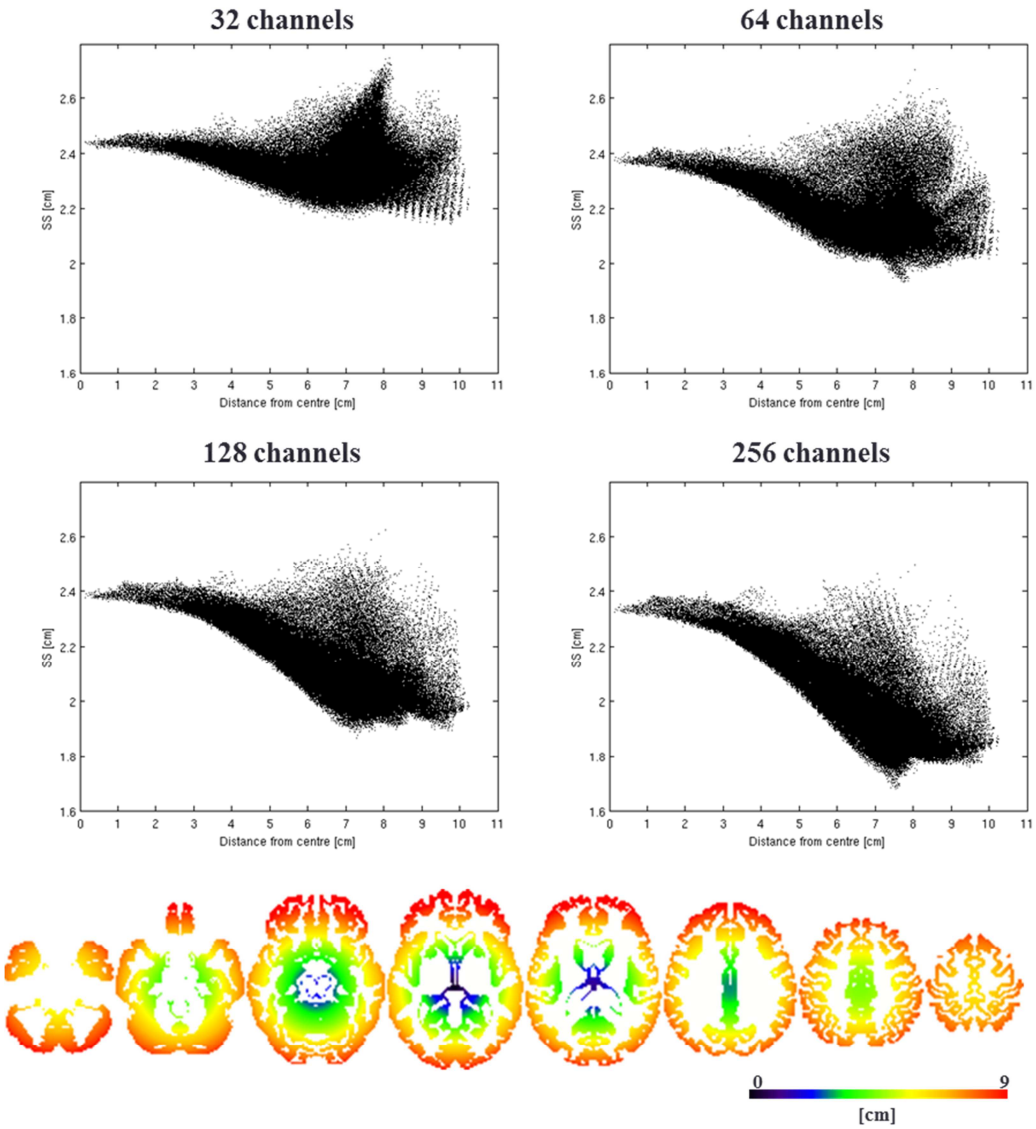

Figure 2.11: Graphs showing, for each EEG montage, the corresponding SS values as a function of the distance of the dipoles from the centre of the head. Last row shows in a color-scale the distance with respect of the centre of the head of each dipole position (see colorbar in the bottom right corner of the figure).

Distributions of Spatial Spread across dipoles position as a function of the number of channels were presented in figure 2.12. Patterns were broadly similar across electrodes configuration. In particular, whereas 64, 128 and 256 channels montage showed a clear radial distribution with the highest spread values located in the deepest positions, with 32 electrodes there were also some peripheral regions with high SS values. By reading the figure by columns, it can be seen that solutions became less widely distributed with a larger number of electrodes.

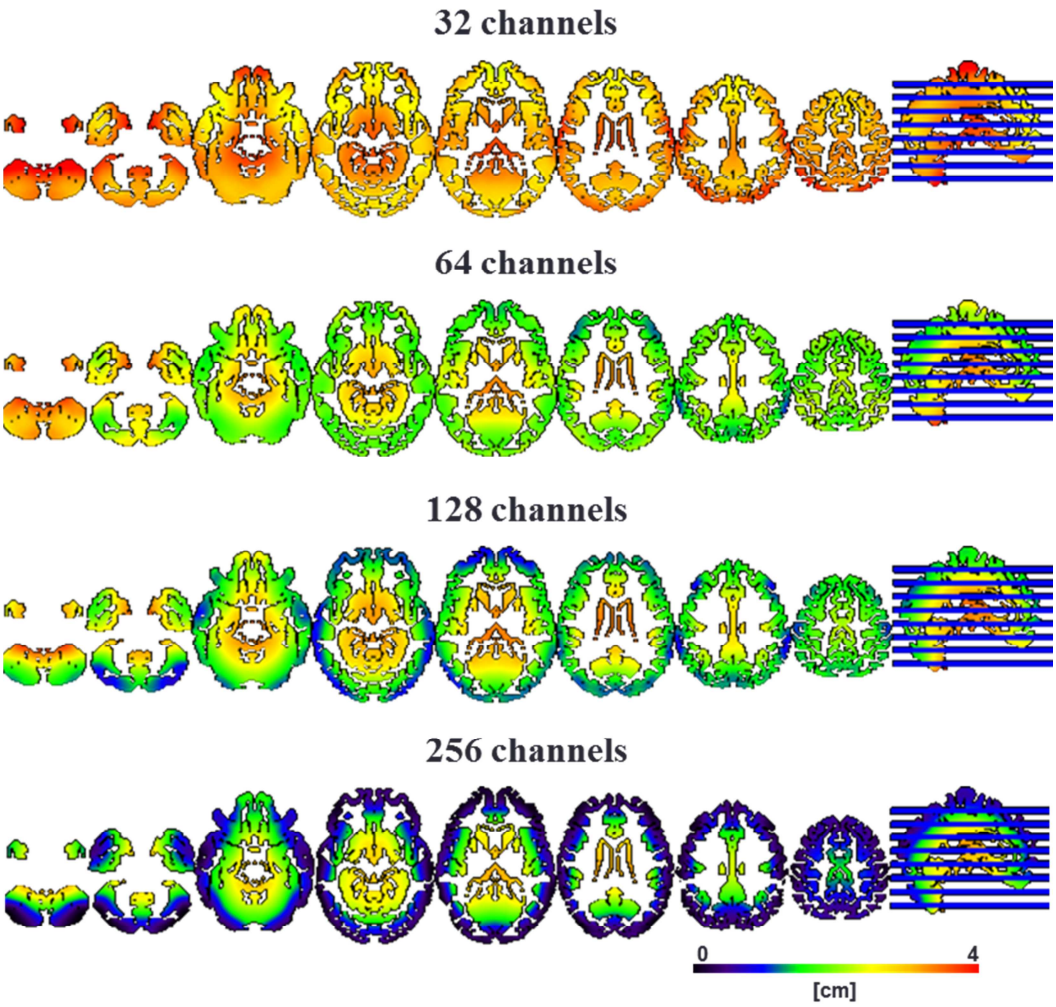

Figure 2.12: Spatial maps showing, in a color-scale, the brain distribution of SS values for each EEG montage (see colorbar in the bottom right corner of the figure).

As for LE, the Wilcoxon ranksum test revealed that switching from 32 to 64 and from 128 to 256 channels, significant improvements were found all over the brain. In figure 2.13, regions where an increase of electrodes from 64 to 128 did not implicate a significant less spread solution where shown. In particular, comparable results were found in the supramarginal gyrus, the angular gyrus, the primary motor cortex, the lateral prefrontal cortex, the insula, and in the deepest structures and medial cortices.

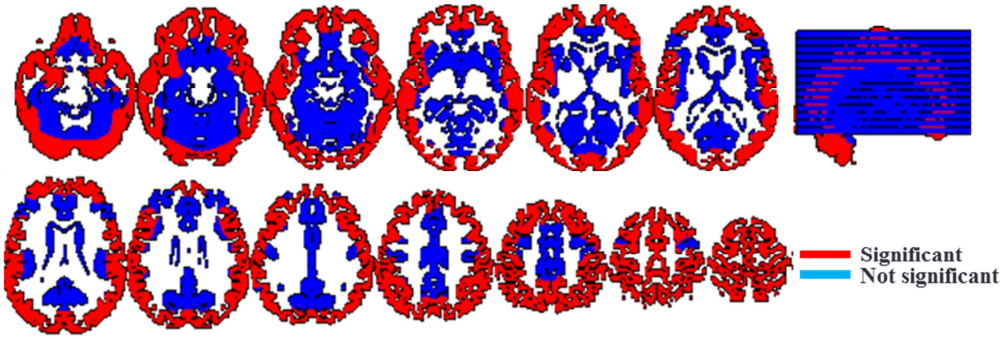

Figure 2.13: Spatial map showing the results of the Wilcoxon runksum test between SS values of the 64-channel montage and 128-channel montage. Blue color indicates the cortical brain regions in which SS values did not significantly decrease moving from the 64-channel to 128-channel montage.

Concerning the median distance of the dipole for all the electrodes, as can be seen in figure 2.14, only 256 channels montage showed a monotonic decrease of SS as a function of this metric.

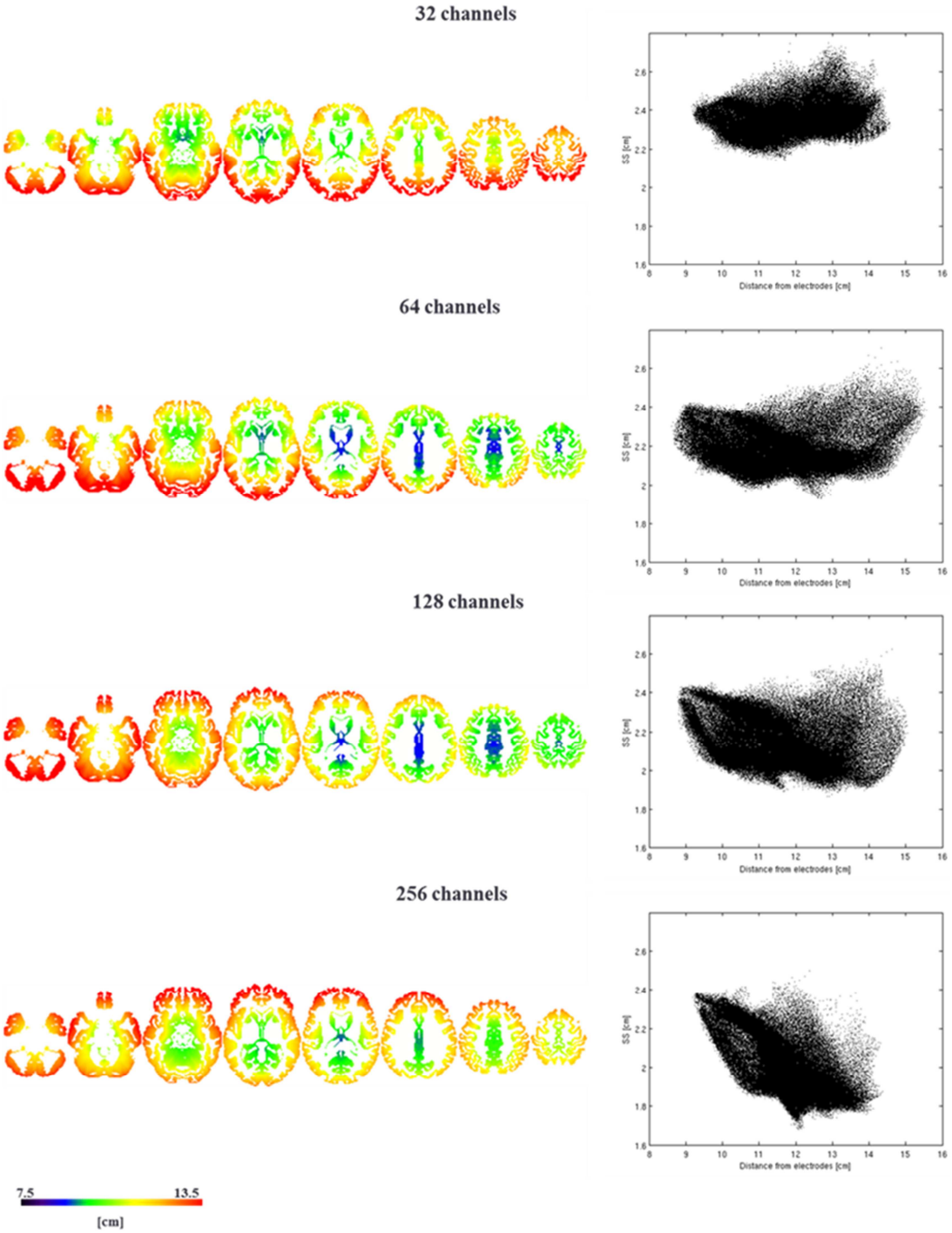

Figure 2.14: The right column of the figure shows, for each EEG montage, the corresponding SS values as a function of the median dipoles distance from all the electrodes (Distance from electrodes) (see colorbar in the bottom left of the figure). The left column shows, for each montage, the brain distribution of this latter measure . Note that spatial profile changes with the EEG montage.

2.9 Discussion

It is now generally accepted that the accuracy of EEG source reconstruction depends on several factors such as the EEG electrodes montage, the degree of approximation considered to build the head model, and the algorithm used to solve the inverse problem (for reviews see Michel et al. 2004, Hallez et al. 2007). However, all the existing (non-clinical) studies investigating the factors affecting EEG source reconstruction accuracy only reported the mean localization errors averaged across dipoles throughout the whole brain. To the best of our knowledge, thus, it still remains to be investigated in details how source localization accuracy is distributed across the brain, as well as the impact of EEG sensors density and configurations. The present study aimed to fill this gap. Here, source localization performances with simulated data on 32-, 64-, 128-, and 256-channel EEG montages were compared in order to investigate the effect of channel configuration on source estimation. Importantly, in the present study the gold standard techniques for both the head model description and the inverse problem solution were used.

Concerning the head model, a very computationally efficient solution consists in modelling the head as three or four concentric spherical shells representing scalp, skull, cerebrospinal fluid and brain, a solution that has been widely used in earlier source reconstruction studies (Sun 1997, Cuffin and Cohen 1979, Rush and Driscoll 1968, Stok 1987). However several studies highlighted that these representations produced relatively poor results (Zhang and Jewett 1993, Yvert et al. 1997) because they do not take into account the thickness and curvature of the skull (Cuffin 1993, Chauveau et al. 2004), and the geometry of the head (Roth et al. 1993, Roth et al. 1997, Huiskamp et al. 1999). Better performance could instead be achieved with more realistic descriptions of the head tissues (Vatta et al. 2010, Akalin Acar and Makeig 2013, Ramon, Schimpf and Haueisen 2006) using the boundary element method (Akalin-Acar and Gencer 2004), finite element method (Gencer and Acar 2004, Wolters et al. 2002) or finite difference method (Vanrumste et al. 2000). Concerning how many tissues should be accounted for in

such realistic description, previous studies demonstrated that the accuracy of the source estimation benefited from distinguishing white and grey matter tissues (Akalin Acar and Makeig 2013, Van Uitert, Johnson and Zhukov 2004), from distinguishing compact and spongy bone tissues composing the skull (Dannhauer et al. 2011, Montes-Restrepo et al. 2013) and from adding a compartment for CSF (Akalin Acar and Makeig 2013, Hyde, Duffy and Warfield 2012, Lanfer et al. 2012). Based on these findings, thus, 12 tissues were here considered in order to give an as detailed as possible description of the head.

As regard the inverse problem solution, several studies (Pascual-Marqui 2002, Grech et al. 2008, Song et al. 2015) showed that sLORETA (Pascual-Marqui 2002), gives the more accurate solution when localizing a single source as compared to other parametric algorithm commonly used. In this study, source estimation was not computed with this technique, but rather with its improvement version, eLORETA. This method was proved to produce clearer and less blurred solutions as compared to sLORETA (Jatoi et al. 2014, Pascual-Marqui et al. 2011).

A first result of the present study, as revealed by the simulation employed here, is that performance on source estimation improved with increasing the number of electrodes, as expected based on previous works (Michel et al. 2004, Lantz et al. 2003, Song et al. 2015, Sohrabpour et al. 2015). Specifically, as shown in figure 2.4, the analyses revealed that the median of the localization errors exponentially decreased as function of the number of electrodes used in the simulation. Although in the above-mentioned studies (Sohrabpour et al. 2015, Song et al. 2015, Lantz et al. 2003) the fit was not provided, those authors also qualitatively observed that the rate of localization errors reduction decreased as montage spatial sampling increased.

A second, related, result of the present study is illustrated in figure 2.5, which shows, for each montage, the relationship between localization errors and the dipole positions with respect to the centre of the head. This plot clearly indicates that, in each configuration, the decay of the localization error as a function of the

dipole location (relative to the head centre) followed a sigmoid function, thus indicating higher localization errors for deeper sources as compared to more shallow ones. This is in line with the pattern of worst localizations for deeper sources that has already been observed in several studies in which different head models, electrodes configurations and inverse problem solutions were adopted (e.g., Dale and Sereno 1993, Grave de Peralta-Menendez and Gonzalez-Andino 1998, Sohrabpour et al. 2015).

It is important here to remark that existing studies usually provided performances assessment considering all the dipoles together, without took into account their relative position in the grey matter. In this work, instead, the improvement in source estimation with increasing number of electrodes was evaluated for each source. It was found that all the sources were better localized (FDR corrected, $p < 0.05$) with 64 channels as compared to 32 channels, whereas moving from 64 to 128 channels favored, in general, only shallow sources (see figure 2.7). In literature there are not studies to which compare these latter results. As regard the whole brain improvement from 32 to 64 electrodes, it could be explained considering the big LE decay observed in Lantz et al. (2003), Sohrabpour et al. (2015) and Song et al. (2015) when using 64 channels montage in place of a lower density montage. Concerning the regional improvement from 64 to 128, it could be justified considering that the mean marginal improvement observed in Lantz et al. (2003), Sohrabpour et al. (2015) and Song et al. (2015) from 64 to 128 channels could be due to better performance in the more superficial sources and comparable performance in the deeper sources. Unexpectedly, significant better performances all over the brain were also found in the present study with 256 channels montage as compared to 128 channels one. However, this result should be considered in light of the observed effect size and, especially, the entire distribution of localization error across the brain. Indeed, the figure 2.3 show that the difference between medians of localization errors of 256 channels and 128 channels configurations was in the order of few millimeters, and the brain maps of localization errors for these EEG montages are very similar.

It is worth noting the limitations of the present study. First of all, performances were evaluated without taking into account typical artifacts that usually corrupted EEG data, e.g., the muscular activity that predominantly affects the recordings in the lower regions of the head and in the neck, and the ocular artifacts that mainly interest the electrodes over the face. Solution of the inverse problem from noisy data could become inaccurate resulting in a regional or whole brain decline of the estimate performances. Another limitation of the study is that the accuracy of the source reconstruction was assessed based on the ability to localize the activity of a single point source, which is physiologically not plausible. It would be thus important evaluating localization error both in the presence of multiple point sources at different distances between each other, and in the presence of distributed sources, as well as the interaction between these factor and the regularization parameter. Also, a confirmatory study with real data could be useful. For example, several fMRI studies have shown that median nerve stimulation activate somatosensory cortex and insula (Francis et al. 2000, Ferretti et al. 2004, Del Gratta et al. 2000), two regions that showed very different performances as function of the number of electrodes (see figure 2.6). To confirm our results, the source reconstruction computed on EEG data acquired during this simulation should be able to localize with high accuracy the somatomotor cortex starting from 64 electrodes configuration, but the accurate localization of the insular sources should be achieved only using 128- or 256-channel montages.

In conclusion, taken together the present results highlight the importance of using at least 64 channels to achieve an acceptable accuracy on source reconstruction. Moreover, regardless the number of electrodes, it was shown that accuracy strongly depend on the position of the sources in the head. This evidence suggested that the decision about how many electrodes are needed to obtain an accurate solution should be pondered based on the localization of the region of interest involved in the experiment. For example, if the area of interest is in the parietal lobe, an EEG montage with 64 channels is enough to localize that region with an error lower than 1 cm; by contrast, in order to obtain the same accuracy in other regions of the brain, a 256 channel montage would be needed.

3 Conclusion

To date, the functional role of the fluctuations of the fMRI signal at rest is still not clear, mainly because their neuronal basis are yet to be elucidated. In this scenario, the integration with information derived from electroencephalography (EEG) is very useful, since conversely from fMRI, EEG represents a direct measure of neuronal activity. Therefore, a first resting state EEG-fMRI study was conducted with the aim to identify specific spatio-spectral fingerprints of distinct resting state networks. With this aim, an analytical approach was used that allows to take into account the interplay between the different EEG frequency bands and the corresponding topographic distribution within each network. Specifically, this approach was applied to four sub-components of the Default Mode Network (DMN).

Results of the first study revealed for the first time that the scalp distribution of the EEG spectral correlates of fMRI RSNs provides a rich source of information about the physiological underpinnings and the functional characterization of the different (subcomponent of the) RSNs. In particular, more detailed analyses allowed to identify some putative specific spatio-spectral fingerprints of distinct (subcomponent of the) RSNs. These results highlight the importance to take into account the interplay between different EEG frequency bands, and the corresponding topographic distribution, in future EEG-fMRI integration studies.

However, the spatial resolution of the EEG signal is too low to reliably infer about the location of the involved EEG sources, and it is not clear whether the 64 channels EEG system employed in the first study can provide adequate performance in localizing the related cortical sources. Therefore, an investigation

of the source reconstruction accuracy throughout the brain with different EEG montages was performed in a second simulation study.

Results of this second study showed the general superiority of 256-channel montage with respect to lower density EEG montages in enabling accurate source localizations. Moreover, analysis showed that the improvement of the performances moving from 128 channels to 256 channels is modest, and that some regions does not show significant improvement switching from 64 channels to 128 channels. Therefore, the take-home message is that at least 64 channels should be used, and would be adequate in most cases, to achieve an acceptable accuracy on source reconstruction. An attempt to extend the first resting state coregistration study with the source reconstruction could be workable, although a confirmation study with a 128-, or even 256-, channel montage is needed, especially to infer about the deep midline regions.

4 Bibliography

Akalin Acar, Z. & S. Makeig. 2013. Effects of Forward Model Errors on EEG Source Localization. In *Brain Topogr*, 378-96.

Akalin-Acar, Z. & N. G. Gencer (2004) An advanced boundary element method (BEM) implementation for the forward problem of electromagnetic source imaging. *Phys Med Biol,* 49**,** 5011-28.

Allen, E. A., E. Damaraju, S. M. Plis, E. B. Erhardt, T. Eichele & V. D. Calhoun (2014) Tracking whole-brain connectivity dynamics in the resting state. *Cereb Cortex,* 24**,** 663-76.

Allen, P. J., O. Josephs & R. Turner (2000) A method for removing imaging artifact from continuous EEG recorded during functional MRI. *Neuroimage,* 12**,** 230-239.

Ambrosini, E. & A. Vallesi (2016) Asymmetry in prefrontal resting-state EEG spectral power underlies individual differences in phasic and sustained cognitive control. *Neuroimage,* 124**,** 843-857.

Andrews-Hanna, J. R., J. S. Reidler, J. Sepulcre, R. Poulin & R. L. Buckner (2010) Functional-anatomic fractionation of the brain's default network. *Neuron,* 65**,** 550-62.

Babiloni, F., F. Cincotti, F. Carducci, P. M. Rossini & C. Babiloni. 2001. Spatial enhancement of EEG data by surface Laplacian estimation: the use of magnetic resonance imaging-based head models. In *Clin Neurophysiol*, 724-7. Netherlands.

Baillet, S. & L. Garnero (1997) A Bayesian approach to introducing anatomo-functional priors in the EEG/MEG inverse problem. *IEEE Trans Biomed Eng,* 44**,** 374-85.

Beckmann, C. F., M. DeLuca, J. T. Devlin & S. M. Smith (2005) Investigations into resting-state connectivity using independent component analysis. *Philos Trans R Soc Lond B Biol Sci,* 360**,** 1001-13.

Bell, A. J. & T. J. Sejnowski (1995) An information-maximization approach to blind separation and blind deconvolution. *Neural Comput,* 7**,** 1129-59.

Berger, H. (1929) Über das elektrenkephalogramm des menschen. *European Archives of Psychiatry and Clinical Neuroscience,* 87**,** 527-570.

Besl, P. J. & N. D. McKay (1992) A method for registration of 3-D shapes. *IEEE Transactions on pattern analysis and machine intelligence,* 14**,** 239-256.

Bigdely-Shamlo, N., T. Mullen, C. Kothe, K. M. Su & K. A. Robbins (2015) The PREP pipeline: standardized preprocessing for large-scale EEG analysis. *Front Neuroinform,* 9**,** 16.

Binder, J. R., J. A. Frost, T. A. Hammeke, P. S. Bellgowan, S. M. Rao & R. W. Cox (1999) Conceptual processing during the conscious resting state. A functional MRI study. *J Cogn Neurosci,* 11**,** 80-95.

Biswal, B., F. Z. Yetkin, V. M. Haughton & J. S. Hyde (1995) Functional connectivity in the motor cortex of resting human brain using echo-planar MRI. *Magn Reson Med,* 34**,** 537-41.

Cavanagh, J. F. & M. J. Frank (2014) Frontal theta as a mechanism for cognitive control. *Trends Cogn Sci,* 18**,** 414-21.

Chauveau, N., X. Franceries, B. Doyon, B. Rigaud, J. P. Morucci & P. Celsis (2004) Effects of skull thickness, anisotropy, and inhomogeneity on forward EEG/ERP computations using a spherical three-dimensional resistor mesh model. *Hum Brain Mapp,* 21**,** 86-97.

Cohen, D. & B. N. Cuffin (1983) Demonstration of useful differences between magnetoencephalogram and electroencephalogram. *Electroencephalogr Clin Neurophysiol,* 56**,** 38-51.

Cohen, M. X. & T. H. Donner (2013) Midfrontal conflict-related theta-band power reflects neural oscillations that predict behavior.

Cole, D. M., D. o. C. N. Imperial College London, London, United Kingdom, dcole.neurosci@gmail.com, S. M. Smith, D. o. C. N. University of Oxford, Oxford, United Kingdom, steve@fmrib.ox.ac.uk, C. F. Beckmann, D. o. C. N. Imperial College London, London, United Kingdom, D. o. C. N. University of Oxford, Oxford, United Kingdom & c.beckmann@donders.ru.nl (2010) Advances and pitfalls in the analysis and interpretation of resting-state FMRI data. *Frontiers in Systems Neuroscience,* 4.

Cordes, D., V. M. Haughton, K. Arfanakis, J. D. Carew, P. A. Turski, C. H. Moritz, M. A. Quigley & M. E. Meyerand (2001) Frequencies contributing to functional connectivity in the cerebral cortex in "resting-state" data. *AJNR Am J Neuroradiol,* 22**,** 1326-33.

Cuffin, B. N. (1993) Effects of local variations in skull and scalp thickness on EEG's and MEG's. *IEEE Trans Biomed Eng,* 40**,** 42-8.

Cuffin, B. N. & D. Cohen (1979) Comparison of the magnetoencephalogram and electroencephalogram. *Electroencephalogr Clin Neurophysiol,* 47**,** 132-46.

Dale, A. M. & M. I. Sereno (1993) Improved Localizadon of Cortical Activity by Combining EEG and MEG with MRI Cortical Surface Reconstruction: A Linear Approach. *J Cogn Neurosci,* 5**,** 162-76.

Dannhauer, M., B. Lanfer, C. H. Wolters & T. R. Knosche (2011) Modeling of the human skull in EEG source analysis. *Hum Brain Mapp,* 32**,** 1383-99.

de Munck, J. C., B. W. van Dijk & H. Spekreijse (1988) Mathematical dipoles are adequate to describe realistic generators of human brain activity. *IEEE Trans Biomed Eng,* 35**,** 960-6.

Debener, S., A. Strobel, B. Sorger, J. C. Peters, C. Kranczioch, A. Engel & R.Goebel (2007) Improved quality of auditory event-related potentials recorded simultaneously with 3-T fMRI: removal of the ballistocardiogram artefact. *Neuroimage,* 34**,** 587-597.

Debener, S., M. Ullsperger, M. Siegel, K. Fiehler, D. Y. v. Cramon & A. K. Engel (2005) Trial-by-Trial Coupling of Concurrent Electroencephalogram and Functional Magnetic Resonance Imaging Identifies the Dynamics of Performance Monitoring.

Del Gratta, C., S. Della Penna, A. Tartaro, A. Ferretti, K. Torquati, L. Bonomo, G. L. Romani & P. M. Rossini (2000) Topographic organization of the human primary and secondary somatosensory areas: an fMRI study. *Neuroreport,* 11**,** 2035-43.

Delorme, A. & S. Makeig (2004) EEGLAB: an open source toolbox for analysis of single-trial EEG dynamics including independent component analysis. *J Neurosci Methods,* 134**,** 9-21.

Feige, B., K. Scheffler, F. Esposito, F. Di Salle, J. Hennig & E. Seifritz (2005) Cortical and subcortical correlates of electroencephalographic alpha rhythm modulation. *J Neurophysiol,* 93**,** 2864-72.

Ferretti, A., C. Del Gratta, C. Babiloni, M. Caulo, D. Arienzo, A. Tartaro, P. M. Rossini & G. L. Romani (2004) Functional topography of the secondary somatosensory cortex for nonpainful and painful stimulation of median and tibial nerve: an fMRI study. *Neuroimage,* 23**,** 1217-25.

Filippini, N., B. J. MacIntosh, M. G. Hough, G. M. Goodwin, G. B. Frisoni, S. M. Smith, P. M. Matthews, C. F. Beckmann & C. E. Mackay (2009) Distinct patterns of brain activity in young carriers of the APOE-epsilon4 allele. *Proc Natl Acad Sci U S A,* 106**,** 7209-14.

Fischl, B. (2012) FreeSurfer. *Neuroimage,* 62**,** 774-81.

Fox, M. D. & M. E. Raichle (2007) Spontaneous fluctuations in brain activity observed with functional magnetic resonance imaging. *Nature Reviews Neuroscience,* 8**,** 700-711.

Francis, S., E. Kelly, R. Bowtell, W. Dunseath, S. Folger & F. McGlone (2000) fMRI of the responses to vibratory stimulation of digit tips. *Neuroimage,* 11**,** 188-202.

Freeman, W. J., M. D. Holmes, B. C. Burke & S. Vanhatalo (2003) Spatial spectra of scalp EEG and EMG from awake humans. *Clin Neurophysiol,* 114**,** 1053-68.

Friston, K. J. (1994) Functional and effective connectivity in neuroimaging: a synthesis. *Human brain mapping,* 2**,** 56-78.

Friston, K. J., C. D. Frith, P. Fletcher, P. F. Liddle & R. S. Frackowiak (1996) Functional topography: multidimensional scaling and functional connectivity in the brain. *Cereb Cortex,* 6**,** 156-64.

Fuchs, M., M. Wagner & J. Kastner (2001) Boundary element method volume conductor models for EEG source reconstruction. *Clin Neurophysiol,* 112**,** 1400-7.

Garreffa, G., M. Bianciardi, G. E. Hagberg, E. Macaluso, M. G. Marciani, B. Maraviglia, M. Abbafati, M. Carni, I. Bruni & L. Bianchi (2004) Simultaneous EEG-fMRI acquisition: how far is it from being a standardized technique? *Magn Reson Imaging,* 22**,** 1445-55.

Gavit, L., S. Baillet, J. F. Mangin, J. Pescatore & L. Garnero (2001) A multiresolution framework to MEG/EEG source imaging. *IEEE Trans Biomed Eng,* 48**,** 1080-7.

Gencer, N. G. & C. E. Acar (2004) Sensitivity of EEG and MEG measurements to tissue conductivity. *Phys Med Biol,* 49**,** 701-17.

Goldman, R., J. Stern, J. Engel & M. Cohen (2001) Tomographic mapping of alpha rhythm using simultaneous EEG/fMRI. *NeuroImage,* 6**,** 1291.

Goldman, R. I., J. M. Stern, J. Engel & M. S. Cohen (2002) Simultaneous EEG and fMRI of the alpha rhythm. *Neuroreport,* 13**,** 2487-92.

Goncalves, S. I., J. C. de Munck, P. J. Pouwels, R. Schoonhoven, J. P. Kuijer, N. M. Maurits, J. M. Hoogduin, E. J. Van Someren, R. M. Heethaar & F. H. Lopes da Silva (2006) Correlating the alpha rhythm to BOLD using simultaneous EEG/fMRI: inter-subject variability. *Neuroimage,* 30**,** 203-13.

Grave de Peralta Menendez, R., S. Gonzalez Andino, G. Lantz, C. M. Michel & T. Landis (2001) Noninvasive localization of electromagnetic epileptic activity. I. Method descriptions and simulations. *Brain Topogr,* 14**,** 131-7.

Grave de Peralta-Menendez, R. & S. L. Gonzalez-Andino (1998) A critical analysis of linear inverse solutions to the neuroelectromagnetic inverse problem. *IEEE Trans Biomed Eng,* 45**,** 440-8.

Grech, R., T. Cassar, J. Muscat, K. P. Camilleri, S. G. Fabri, M. Zervakis, P. Xanthopoulos, V. Sakkalis & B. Vanrumste (2008) Review on solving the inverse problem in EEG source analysis. *Journal of neuroengineering and rehabilitation,* 5**,** 25.

Greicius, M. D., B. H. Flores, V. Menon, G. H. Glover, H. B. Solvason, H. Kenna, A. L. Reiss & A. F. Schatzberg (2007) Resting-state functional connectivity in major depression: abnormally increased contributions from subgenual cingulate cortex and thalamus. *Biol Psychiatry,* 62**,** 429-37.

Greicius, M. D., B. Krasnow, A. L. Reiss & V. Menon (2003) Functional connectivity in the resting brain: a network analysis of the default mode hypothesis. *Proc Natl Acad Sci U S A,* 100**,** 253-8.

Greicius, M. D., G. Srivastava, A. L. Reiss & V. Menon (2004) Default-mode network activity distinguishes Alzheimer's disease from healthy aging: evidence from functional MRI. *Proc Natl Acad Sci U S A,* 101**,** 4637-42.

Hallez, H., B. Vanrumste, R. Grech, J. Muscat, W. De Clercq, A. Vergult, Y. D'Asseler, K. P. Camilleri, S. G. Fabri, S. Van Huffel & I. Lemahieu. 2007. Review on solving the forward problem in EEG source analysis. In *J Neuroeng Rehabil*, 46.

Haueisen, J., C. Ramon, M. Eiselt, H. Brauer & H. Nowak (1997) Influence of tissue resistivities on neuromagnetic fields and electric potentials studied with a finite element model of the head. *IEEE Trans Biomed Eng,* 44**,** 727-35.

Hauk, O., D. G. Wakeman & R. Henson (2011) Comparison of noise-normalized minimum norm estimates for MEG analysis using multiple resolution metrics. *Neuroimage,* 54**,** 1966-74.

Heine, L., A. Soddu, F. Gómez, A. Vanhaudenhuyse, L. Tshibanda, M. Thonnard, V. Charland-Verville, M. Kirsch, S. Laureys & A. Demertzi (2012) Resting State Networks and Consciousness: Alterations of Multiple Resting State Network Connectivity in Physiological, Pharmacological, and Pathological Consciousness States. *Front Psychol,* 3.

Hill, R. A., K. H. Chiappa, F. Huang-Hellinger & B. G. Jenkins (1995) EEG during MR imaging: differentiation of movement artifact from paroxysmal cortical activity. *Neurology,* 45**,** 1942-3.

Himberg, J., A. Hyvarinen & F. Esposito (2004) Validating the independent components of neuroimaging time series via clustering and visualization. *Neuroimage,* 22**,** 1214-22.

Holmes, C. J., R. Hoge, L. Collins, R. Woods, A. W. Toga & A. C. Evans (1998) Enhancement of MR images using registration for signal averaging. *J Comput Assist Tomogr,* 22**,** 324-33.

Huiskamp, G., M. Vroeijenstijn, R. van Dijk, G. Wieneke & A. C. van Huffelen (1999) The need for correct realistic geometry in the inverse EEG problem. *IEEE Transactions on Biomedical Engineering,* 46**,** 1281-1287.

Hyde, D. E., F. H. Duffy & S. K. Warfield (2012) Anisotropic partial volume CSF modeling for EEG source localization. *Neuroimage,* 62**,** 2161-70.

Iacono, M. I., E. Neufeld, E. Akinnagbe, K. Bower, J. Wolf, I. Vogiatzis Oikonomidis, D. Sharma, B. Lloyd, B. J. Wilm, M. Wyss, K. P. Pruessmann, A. Jakab, N. Makris, E. D. Cohen, N. Kuster, W. Kainz & L. M. Angelone (2015) MIDA: A Multimodal Imaging-Based Detailed Anatomical Model of the Human Head and Neck. *PLoS One,* 10**,** e0124126.

Iannotti, G. R., F. Pittau, C. M. Michel, S. Vulliemoz & F. Grouiller (2015) Pulse artifact detection in simultaneous EEG-fMRI recording based on EEG map topography. *Brain Topogr,* 28**,** 21-32.

Jann, K., T. Dierks, C. Boesch, M. Kottlow, W. Strik & T. Koenig (2009) BOLD correlates of EEG alpha phase-locking and the fMRI default mode network. *Neuroimage,* 45**,** 903-916.

Jann, K., M. Kottlow, T. Dierks, C. Boesch & T. Koenig (2010) Topographic electrophysiological signatures of fMRI resting state networks. *PloS one,* 5**,** e12945.

Jatoi, M. A., N. Kamel, A. S. Malik & I. Faye (2014) EEG based brain source localization comparison of sLORETA and eLORETA. *Australas Phys Eng Sci Med,* 37**,** 713-21.

Jerbi, K., J. R. Vidal, T. Ossandon, S. S. Dalal, J. Jung, D. Hoffmann, L. Minotti, O. Bertrand, P. Kahane & J. P. Lachaux (2010) Exploring the Electrophysiological Correlates of the Default-Mode Network with Intracerebral EEG. *Front Syst Neurosci,* 4.

Johnson, S. C. (1967) Hierarchical clustering schemes. *Psychometrika,* 32**,** 241-254.

Kennerley, A. J., J. E. Mayhew, P. Redgrave & J. Berwick. 2010. Vascular Origins of BOLD and CBV fMRI Signals: Statistical Mapping and Histological Sections Compared. In *Open Neuroimag J*, 1-8.

Kochiyama, T., T. Morita, T. Okada, Y. Yonekura, M. Matsumura & N. Sadato (2005) Removing the effects of task-related motion using independent-component analysis. *Neuroimage,* 25**,** 802-14.

Koenig, T. & L. Melie-Garcia (2009) q 4 Statistical analysis of multichannel'scalp field data. *Electrical neuroimaging***,** 169.

Koenig, T., L. Melie-Garcia, M. Stein, W. Strik & C. Lehmann (2008) Establishing correlations of scalp field maps with other experimental variables using covariance analysis and resampling methods. *Clin Neurophysiol,* 119**,** 1262-70.

Laarne, P. H., M. L. Tenhunen-Eskelinen, J. K. Hyttinen & H. J. Eskola (2000) Effect of EEG electrode density on dipole localization accuracy using two realistically shaped skull resistivity models. *Brain Topogr,* 12**,** 249-54.

Lanfer, B., I. Paul-Jordanov, M. Scherg & C. H. Wolters (2012) Influence of interior cerebrospinal fluid compartments on EEG source analysis. *Biomedical Engineering/Biomedizinische Technik,* 57**,** 236-236.

Lantz, G., R. Grave de Peralta Menendez, S. Gonzalez Andino & C. M. Michel (2001) Noninvasive localization of electromagnetic epileptic activity. II.

Demonstration of sublobar accuracy in patients with simultaneous surface and depth recordings. *Brain Topogr,* 14**,** 139-47.

Lantz, G., R. Grave de Peralta, L. Spinelli, M. Seeck & C. M. Michel (2003) Epileptic source localization with high density EEG: how many electrodes are needed? *Clin Neurophysiol,* 114**,** 63-9.

Laufs, H. (2008) Endogenous brain oscillations and related networks detected by surface EEG-combined fMRI. *Hum Brain Mapp,* 29**,** 762-9.

Laufs, H., J. L. Holt, R. Elfont, M. Krams, J. S. Paul, K. Krakow & A. Kleinschmidt (2006) Where the BOLD signal goes when alpha EEG leaves. *Neuroimage,* 31**,** 1408-18.

Laufs, H., A. Kleinschmidt, A. Beyerle, E. Eger, A. Salek-Haddadi, C. Preibisch & K. Krakow (2003a) EEG-correlated fMRI of human alpha activity. *Neuroimage,* 19**,** 1463-1476.

Laufs, H., K. Krakow, P. Sterzer, E. Eger, A. Beyerle, A. Salek-Haddadi & A. Kleinschmidt (2003b) Electroencephalographic signatures of attentional and cognitive default modes in spontaneous brain activity fluctuations at rest.

Lavallee, C. F., C. S. Herrmann, R. Weerda & R. J. Huster (2014) Stimulus-response mappings shape inhibition processes: a combined EEG-fMRI study of contextual stopping. *PloS one,* 9**,** e96159.

Lemieux, L., P. J. Allen, F. Franconi, M. R. Symms & D. R. Fish (1997) Recording of EEG during fMRI experiments: patient safety. *Magn Reson Med,* 38**,** 943-52.

Li, Y. O., T. Adali & V. D. Calhoun (2007) Estimating the number of independent components for functional magnetic resonance imaging data. *Hum Brain Mapp,* 28**,** 1251-66.

Liu, Q., S. Farahibozorg, C. Porcaro, N. Wenderoth & D. Mantini (2017) Detecting large-scale networks in the human brain using high-density electroencephalography. *Hum Brain Mapp,* 38**,** 4631-4643.

Logothetis, N. K., J. Pauls, M. Augath, T. Trinath & A. Oeltermann (2001) Neurophysiological investigation of the basis of the fMRI signal. *Nature,* 412**,** 150-157.

Lu, Y., L. Yang, G. A. Worrell & B. He (2012) Seizure source imaging by means of FINE spatio-temporal dipole localization and directed transfer function in partial epilepsy patients. *Clin Neurophysiol,* 123**,** 1275-83.

Mantini, D., S. Della Penna, L. Marzetti, F. de Pasquale, V. Pizzella, M. Corbetta & G. L. Romani (2011a) A signal-processing pipeline for magnetoencephalography resting-state networks. *Brain Connect,* 1**,** 49-59.

Mantini, D., A. Gerits, K. Nelissen, J. B. Durand, O. Joly, L. Simone, H. Sawamura, C. Wardak, G. A. Orban, R. L. Buckner & W. Vanduffel (2011b) Default Mode of Brain Function in Monkeys. *J Neurosci,* 31**,** 12954-62.

Mantini, D., M. G. Perrucci, S. Cugini, A. Ferretti, G. L. Romani & C. Del Gratta (2007a) Complete artifact removal for EEG recorded during continuous fMRI using independent component analysis. *Neuroimage,* 34**,** 598-607.

Mantini, D., M. G. Perrucci, C. Del Gratta, G. L. Romani & M. Corbetta (2007b) Electrophysiological signatures of resting state networks in the human brain. *Proc Natl Acad Sci U S A,* 104**,** 13170-5.

Marino, M., Q. Liu, M. Del Castello, C. Corsi, N. Wenderoth & D. Mantini (2017) Heart-brain interactions in the MR environment: characterization of the ballistocardiogram in EEG signals collected during simultaneous fMRI. *bioRxiv*, 185181.

Mazoyer, B., L. Zago, E. Mellet, S. Bricogne, O. Etard, O. Houde, F. Crivello, M. Joliot, L. Petit & N. Tzourio-Mazoyer (2001) Cortical networks for working memory and executive functions sustain the conscious resting state in man. *Brain Res Bull,* 54**,** 287-98.

McKeown, M. J., L. K. Hansen & T. J. Sejnowsk (2003) Independent component analysis of functional MRI: what is signal and what is noise? *Curr Opin Neurobiol,* 13**,** 620-9.

Mensen, A. & R. Khatami (2013) Advanced EEG analysis using threshold-free cluster-enhancement and non-parametric statistics. *Neuroimage,* 67**,** 111-8.

Michel, C. M., D. Lehmann, B. Henggeler & D. Brandeis (1992) Localization of the sources of EEG delta, theta, alpha and beta frequency bands using the FFT dipole approximation. *Electroencephalogr Clin Neurophysiol,* 82**,** 38-44.

Michel, C. M., M. M. Murray, G. Lantz, S. Gonzalez, L. Spinelli & R. Grave de Peralta (2004) EEG source imaging. *Clin Neurophysiol,* 115**,** 2195-222.

Mo, J., Y. Liu, H. Huang & M. Ding (2013) Coupling between visual alpha oscillations and default mode activity. *Neuroimage,* 68**,** 112-8.

Molins, A., S. M. Stufflebeam, E. N. Brown & M. S. Hamalainen (2008) Quantification of the benefit from integrating MEG and EEG data in minimum l2-norm estimation. *Neuroimage,* 42**,** 1069-77.

Montes-Restrepo, V., P. van Mierlo, J. D. Lopez, H. Hallez & S. Vandenberghe (2013) Influence of isotropic skull models on EEG source localization. *Conf Proc IEEE Eng Med Biol Soc,* 2013**,** 3295-8.

Moosmann, M., P. Ritter, I. Krastel, A. Brink, S. Thees, F. Blankenburg, B. Taskin, H. Obrig & A. Villringer (2003) Correlates of alpha rhythm in functional magnetic resonance imaging and near infrared spectroscopy. *Neuroimage,* 20**,** 145-58.

Mulert, C. & L. Lemieux. 2009. *EEG-fMRI: physiological basis, technique, and applications*. Springer Science & Business Media.

Niazy, R. K., C. F. Beckmann, G. D. Iannetti, J. M. Brady & S. M. Smith (2005) Removal of FMRI environment artifacts from EEG data using optimal basis sets. *Neuroimage,* 28**,** 720-37.

Nunez, P. L. & R. B. Silberstein (2000) On the relationship of synaptic activity to macroscopic measurements: does co-registration of EEG with fMRI make sense? *Brain Topogr,* 13**,** 79-96.

Nunez, P. L. & R. Srinivasan. 2006. *Electric fields of the brain: the neurophysics of EEG*. Oxford University Press, USA.

Nunez, P. L. & A. F. Westdorp (1994) The surface Laplacian, high resolution EEG and controversies. *Brain Topogr,* 6**,** 221-6.

Oehrn, C. R., S. Hanslmayr, J. Fell, L. Deuker, N. A. Kremers, A. T. Do Lam, C. E. Elger & N. Axmacher (2014) Neural communication patterns underlying conflict detection, resolution, and adaptation. *J Neurosci,* 34**,** 10438-52.

Ogawa, S., D. W. Tank, R. Menon, J. M. Ellermann, S. G. Kim, H. Merkle & K. Ugurbil (1992) Intrinsic signal changes accompanying sensory stimulation:

functional brain mapping with magnetic resonance imaging. *Proc Natl Acad Sci U S A,* 89**,** 5951-5.

Oh, S. S., Y. Han, J. Lee, S. D. Yun, J. K. Kang, E. M. Lee, H. W. Yoon, J. Y. Chung & H. Park (2014) A pulse artifact removal method considering artifact variations in the simultaneous recording of EEG and fMRI. *Neurosci Res,* 81-82**,** 42-50.

Oldfield, R. C. (1971) The assessment and analysis of handedness: the Edinburgh inventory. *Neuropsychologia,* 9**,** 97-113.

Oostendorp, T. F., J. Delbeke & D. F. Stegeman (2000) The conductivity of the human skull: results of in vivo and in vitro measurements. *IEEE Trans Biomed Eng,* 47**,** 1487-92.

Pascual-Marqui, R. D. 2002. Standardized low-resolution brain electromagnetic tomography (sLORETA): technical details. In *Methods Find Exp Clin Pharmacol*, 5-12. Spain.

Pascual-Marqui, R. D., D. Lehmann, M. Koukkou, K. Kochi, P. Anderer, B. Saletu, H. Tanaka, K. Hirata, E. R. John & L. Prichep (2011) Assessing interactions in the brain with exact low-resolution electromagnetic tomography. *Philosophical Transactions of the Royal Society of London A: Mathematical, Physical and Engineering Sciences,* 369**,** 3768-3784.

Pasquale, F. d., S. D. Penna, A. Z. Snyder, C. Lewis, D. Mantini, L. Marzetti, P. Belardinelli, L. Ciancetta, V. Pizzella, G. L. Romani & M. Corbetta (2010) Temporal dynamics of spontaneous MEG activity in brain networks.

Perrin, F., J. Pernier, O. Bertrand & J. F. Echallier (1989) Spherical splines for scalp potential and current density mapping. *Electroencephalogr Clin Neurophysiol,* 72**,** 184-7.

Plummer, C., A. S. Harvey & M. Cook (2008) EEG source localization in focal epilepsy: where are we now? *Epilepsia,* 49**,** 201-18.

Popa, D., A. T. Popescu & D. Pare (2009) Contrasting activity profile of two distributed cortical networks as a function of attentional demands. *J Neurosci,* 29**,** 1191-201.

Power, J. D., K. A. Barnes, A. Z. Snyder, B. L. Schlaggar & S. E. Petersen (2012) Spurious but systematic correlations in functional connectivity MRI networks arise from subject motion. *Neuroimage,* 59**,** 2142-54.

Purdon, P. L. & R. M. Weisskoff (1998) Effect of temporal autocorrelation due to physiological noise and stimulus paradigm on voxel-level false-positive rates in fMRI. *Hum Brain Mapp,* 6**,** 239-49.

Raichle, M. E., A. M. MacLeod, A. Z. Snyder, W. J. Powers, D. A. Gusnard & G. L. Shulman (2001) A default mode of brain function. *Proc Natl Acad Sci U S A,* 98**,** 676-82.

Ramon, C., P. H. Schimpf & J. Haueisen. 2006. Influence of head models on EEG simulations and inverse source localizations. In *Biomed Eng Online*, 10.

Ritter, P., R. Becker, C. Graefe & A. Villringer (2007) Evaluating gradient artifact correction of EEG data acquired simultaneously with fMRI. *Magn Reson Imaging,* 25**,** 923-32.

Rombouts, S. A., F. Barkhof, R. Goekoop, C. J. Stam & P. Scheltens (2005) Altered resting state networks in mild cognitive impairment and mild Alzheimer's disease: an fMRI study. *Hum Brain Mapp,* 26**,** 231-9.

Roth, B. J., M. Balish, A. Gorbach & S. Sato (1993) How well does a three-sphere model predict positions of dipoles in a realistically shaped head? *Electroencephalogr Clin Neurophysiol,* 87**,** 175-84.

Roth, B. J., D. Ko, I. R. von Albertini-Carletti, D. Scaffidi & S. Sato (1997) Dipole localization in patients with epilepsy using the relistically shaped head model. *Electroencephalography and clinical Neurophysiology,* 102**,** 159-166.

Rullmann, M., A. Anwander, M. Dannhauer, S. K. Warfield, F. H. Duffy & C. H. Wolters (2009) EEG source analysis of epileptiform activity using a 1 mm anisotropic hexahedra finite element head model. *Neuroimage,* 44**,** 399-410.

Rush, S. & D. A. Driscoll (1968) Current distribution in the brain from surface electrodes. *Anesth Analg,* 47**,** 717-23.

Sasai, S., F. Homae, H. Watanabe, A. T. Sasaki, H. C. Tanabe, N. Sadato & G. Taga (2012) A NIRS-fMRI study of resting state network. *Neuroimage,* 63**,** 179-93.

Scheeringa, R., M. C. Bastiaansen, K. M. Petersson, R. Oostenveld, D. G. Norris & P. Hagoort (2008) Frontal theta EEG activity correlates negatively with the default mode network in resting state. *Int J Psychophysiol,* 67**,** 242-51.

Shulman, G. L., J. A. Fiez, M. Corbetta, R. L. Buckner, F. M. Miezin, M. E. Raichle & S. E. Petersen (1997) Common Blood Flow Changes across Visual Tasks: II. Decreases in Cerebral Cortex. *J Cogn Neurosci,* 9**,** 648-63.

Smith, S. M., P. T. Fox, K. L. Miller, D. C. Glahn, P. M. Fox, C. E. Mackay, N. Filippini, K. E. Watkins, R. Toro, A. R. Laird & C. F. Beckmann (2009) Correspondence of the brain's functional architecture during activation and rest.

Smith, S. M., M. Jenkinson, M. W. Woolrich, C. F. Beckmann, T. E. Behrens, H. Johansen-Berg, P. R. Bannister, M. De Luca, I. Drobnjak & D. E. Flitney (2004) Advances in functional and structural MR image analysis and implementation as FSL. *Neuroimage,* 23**,** S208-S219.

Sohrabpour, A., Y. Lu, P. Kankirawatana, J. Blount, H. Kim & B. He (2015) Effect of EEG electrode number on epileptic source localization in pediatric patients. *Clin Neurophysiol,* 126**,** 472-80.

Song, J., C. Davey, C. Poulsen, P. Luu, S. Turovets, E. Anderson, K. Li & D. Tucker (2015) EEG source localization: Sensor density and head surface coverage. *J Neurosci Methods,* 256**,** 9-21.

Srinivasan, R., P. L. Nunez, D. M. Tucker, R. B. Silberstein & P. J. Cadusch (1996) Spatial sampling and filtering of EEG with spline laplacians to estimate cortical potentials. *Brain Topogr,* 8**,** 355-66.

Srinivasan, R., D. M. Tucker & M. Murias (1998) Estimating the spatial Nyquist of the human EEG. *Behavior Research Methods,* 30**,** 8-19.

Stok, C. J. (1987) The influence of model parameters on EEG/MEG single dipole source estimation. *IEEE Trans Biomed Eng,* 34**,** 289-96.

Strik, W. K., A. J. Fallgatter, D. Brandeis & R. D. Pascual-Marqui (1998) Three-dimensional tomography of event-related potentials during response inhibition: evidence for phasic frontal lobe activation. *Electroencephalogr Clin Neurophysiol,* 108**,** 406-13.

Sun, M. (1997) An efficient algorithm for computing multishell spherical volume conductor models in EEG dipole source localization. *IEEE transactions on biomedical engineering,* 44**,** 1243-1252.

Tarantino, V., I. Mazzonetto, S. Formica, F. Causin & A. Vallesi (2017) The Neural Bases of Event Monitoring across Domains: a Simultaneous ERP-fMRI Study. *Front Hum Neurosci,* 11.

Ullsperger, M. & S. Debener. 2010. *Simultaneous EEG and fMRI: recording, analysis, and application*. Oxford University Press.

van den Heuvel, M. P. & H. E. Hulshoff Pol (2010) Exploring the brain network: a review on resting-state fMRI functional connectivity. *Eur Neuropsychopharmacol,* 20**,** 519-34.

Van Uitert, R., C. Johnson & L. Zhukov (2004) Influence of head tissue conductivity in forward and inverse magnetoencephalographic simulations using realistic head models. *IEEE Trans Biomed Eng,* 51**,** 2129-37.

Vanrumste, B., G. Van Hoey, R. Van de Walle, M. D'Have, I. Lemahieu & P. Boon (2000) Dipole location errors in electroencephalogram source analysis due to volume conductor model errors. *Med Biol Eng Comput,* 38**,** 528-34.

Vatta, F., P. Bruno & P. Inchingolo (2005) Multiregion bicentric-spheres models of the head for the simulation of bioelectric phenomena. *IEEE transactions on biomedical engineering,* 52**,** 384-389.

Vatta, F., F. Meneghini, F. Esposito, S. Mininel & F. D. Salle (2010) Realistic and spherical head modeling for EEG forward problem solution: a comparative cortex-based analysis. *Computational intelligence and neuroscience,* 2010**,** 13.

Viola, F. C., J. Thorne, B. Edmonds, T. Schneider, T. Eichele & S. Debener (2009) Semi-automatic identification of independent components representing EEG artifact. *Clin Neurophysiol,* 120**,** 868-77.

Wang, G., G. Worrell, L. Yang, C. Wilke & B. He (2011) Interictal spike analysis of high-density EEG in patients with partial epilepsy. *Clin Neurophysiol,* 122**,** 1098-105.

Ward Jr, J. H. (1963) Hierarchical grouping to optimize an objective function. *Journal of the American statistical association,* 58**,** 236-244.

Weisskoff, R. M., J. Baker, J. Belliveau, T. L. Davis, K. K. Kwong, M. S. Cohen & B. R. Rosen. 1993. Power spectrum analysis of functionally-weighted MR data: What's 	in the noise? In *12th Annual Scientific Meeting*, 7. New York: Society for Magnetic Resonance in Medicine.

White, B. R., A. Q. Bauer, A. Z. Snyder, B. L. Schlaggar, J. M. Lee & J. P. Culver (2011) Imaging of functional connectivity in the mouse brain. *PLoS One,* 6**,** e16322.

Whitfield-Gabrieli, S., J. M. Moran, A. Nieto-Castanon, C. Triantafyllou, R. Saxe & J. D. Gabrieli (2011) Associations and dissociations between default and self-reference networks in the human brain. *Neuroimage,* 55**,** 225-32.

Whittingstall, K. & N. K. Logothetis (2009) Frequency-band coupling in surface EEG reflects spiking activity in monkey visual cortex. *Neuron,* 64**,** 281-9.

Winkler, I., S. Debener, K. R. Muller & M. Tangermann (2015) On the influence of high-pass filtering on ICA-based artifact reduction in EEG-ERP. *Conf Proc IEEE Eng Med Biol Soc,* 2015**,** 4101-5.

Wolters, C. H., M. Kuhn, A. Anwander & S. Reitzinger (2002) A parallel algebraic multigrid solver for finite element method based source localization in the human brain. *Computing and visualization in science,* 5**,** 165-177.

Yvert, B., O. Bertrand, M. Thevenet, J. F. Echallier & J. Pernier (1997) A systematic evaluation of the spherical model accuracy in EEG dipole localization. *Electroencephalogr Clin Neurophysiol,* 102**,** 452-9.

Zhang, Y., L. Ding, W. van Drongelen, K. Hecox, D. M. Frim & B. He (2006a) A cortical potential imaging study from simultaneous extra- and intracranial electrical recordings by means of the finite element method. *Neuroimage,* 31**,** 1513-24.

Zhang, Y., W. van Drongelen & B. He (2006b) Estimation of in vivo brain-to-skull conductivity ratio in humans. *Appl Phys Lett,* 89**,** 223903-2239033.

Zhang, Z. & D. L. Jewett (1993) Insidious errors in dipole localization parameters at a single time-point due to model misspecification of number of shells. *Electroencephalogr Clin Neurophysiol,* 88**,** 1-11.